Microporous and Mesoporous Materials 336 (2022) 111863

Contents lists available at ScienceDirect

Microporous and Mesoporous Materials

journal homepage: www.elsevier.com/locate/micromeso

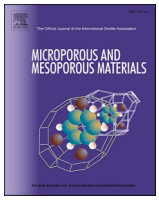

High content and dispersion of Gd in bimodal porous silica: T2 contrast agents under ultra-high magnetic fields☆

M. Dolores Garrido [a], Nuria Puchol [a], Jamal El Haskouri [a,***], Juan Francisco Sánchez-Royo [a], José Vicente Folgado [a], Vannina Gonzalez Marrachelli [b,c], Itziar Pérez Terol [b], José Vicente Ros-Lis [d,**], M. Dolores Marcos [e], Rafael Ruíz [f], Aurelio Beltrán [a], José Manuel Morales [b,g,h], Pedro Amorós [a,*]

[a] Institut de Ciència dels Materials (ICMUV), Universitat de València, P. O. Box 22085, 46071, Valencia, Spain
[b] Laboratory of Metabolomics, Institute of Health Research-INCLIVA, 46010, Valencia, Spain
[c] Department of Physiology, School of Medicine, University of Valencia, 46010, Valencia, Spain
[d] Departamento de Química Inorgánica, Universitat de València, Doctor Moliner 56, 46100, Valencia, Spain
[e] Departamento de Química, Universidad Politécnica de Valencia CIBER de Bioingeniería, Biomateriales y Nanomedicina (CIBER-BBN), Spain
[f] Instituto de Ciència Molecular (ICMol), Universitat de València, Catedrático José Beltrán 2, 46980, Paterna, Valencia, Spain
[g] Unidad Central de Investigación en Medicina, University of Valencia, 46010, Valencia, Spain
[h] Pathology Department, School of Medicine, University of Valencia, 46010, Valencia, Spain

ARTICLE INFO

Keywords:
Mesoporous
Silica
Gadolinium
Magnetic resonance image
Magnetic resonance microscopy

ABSTRACT

Silica-based UVM-7-type bimodal mesoporous materials with high gadolinium content ($\infty \geq Si/Gd \geq 13$) have been synthesized through a one-pot surfactant-assisted procedure from hydroalcoholic solution using a cationic surfactant as template, and starting from atrane complexes of Gd and Si as inorganic precursors. The novel synthetic pathway developed in the study preserves the UVM-7-type architecture while optimizing the dispersion of the Gd-guest species at the nanoscale and even at atomic level. It has been determined that the number of Gd atoms forming clusters is always less than 10. The behaviour under exposure to ultra-high magnetic fields reveals a significant increase in the transversal relaxivity value when compared with related materials in the bibliography. Their activity as T2 instead of T1 contrast agents is discussed and explained considering the high Gd-dispersion and concentration, nature of the materials as well as due to the high magnetic fields used, typical of MRM studies. The absence of toxicity has been confirmed in preliminary cell cultures "in vitro" and the degradation of the solids studied under biological conditions. Results suggest that the atrane route could be a suitable synthesis approach for the preparation of Gd containing contrast agents.

1. Introduction

Magnetic resonance imaging (MRI) is currently one of the most used medical diagnostic modalities. This non-invasive technique provides three-dimensional whole body anatomical imaging with high spatial resolution and almost no limit in penetration depth [1–3]. It exploits the magnetic properties of water protons to distinguish between different organs and/or tissue types. Nevertheless, there are situations where the contrast between adjacent tissues are not strong enough to allow clear discriminations or to enable the observation of fine details. The contrast can be further improved by using non-therapeutic diagnostic compounds known as chemical contrast agents (CA). A CA provides image contrast by shortening both the local longitudinal (T1) and transverse (T2) relaxation times of the protons compared to the surrounding tissue [4]. The ability of a CA to effectively enhance the image contrast is measured as the longitudinal (r1) and transverse (r2) relaxivity values. An effective MRI contrast agent must have a relatively large relaxivity value, r1 (positive T1 CA) or r2 (negative T2 CA) [5,6]. T1 CA, based on

☆ Dedicated to the memory of Professor Saúl Cabrera Medina.

* Corresponding author.
** Corresponding author.
*** Corresponding author.
E-mail addresses: haskouri@uv.es (J. El Haskouri), J.Vicente.Ros@uv.es (J.V. Ros-Lis), pedro.amoros@uv.es (P. Amorós).

https://doi.org/10.1016/j.micromeso.2022.111863
Received 19 January 2022; Received in revised form 7 March 2022; Accepted 20 March 2022
Available online 27 March 2022

paramagnetic species such as Gd(III) and Mn(II) that affect neighboring protons through spin–lattice relaxation, produce positive (bright) image contrast [7,8]. The Gd(III) is the most commonly used paramagnetic ion because of its large magnetic moment with a long electron spin relaxation time [9]. However, free Gd(III) ions are highly toxic. Hence, Gd(III) ions are conventionally sequestered by chelation (with ligands such as DTPA, DOTA) [10] or encapsulation [11,12] in order to reduce their toxicity. Chelation decreases the toxicity of Gd(III) but at the same time reduces the relaxivity as it limits the number of coordination sites accessible for water exchange. In practice, commercial T1 CAs are usually highly stable gadolinium complexes that suffer from low relaxivity (r1 ~ 3 $mM^{-1}s^{-1}$ at 4.7 T), rapid renal clearance, and lack of tissue specificity, thus providing contrast enhancement which is well below the theoretical maximum limit [13]. In addition to chelates, a huge variety of platforms (viral nanoparticles, protein-based agents, micelles and liposomes, dendrimers, gold nanoparticles, carbon-based nanoparticles and nano-tubes, etc.) are currently undergoing development and testing as MRI contrast agents [14–16]. On the other hand, T2-weighted images, based on superparamagnetic iron oxide particles that locally modify the spin–spin relaxation process of water protons, produce negative or dark images [6].

In contrast to the T2 CA type, solid materials have played an almost testimonial role dealing with T1 CAs. Here, we can refer to the studies devoted to Gd_2O_3, $GdPO_4$ modified/protected with other inorganic or organic species [17–23]. In other cases, Gd species, Gd_2O_3 and related nanoparticles have been conveniently dispersed on or within different supports. Thus, dextran coated gadolinium-doped CeO_2 NPs with high T1 relaxivity values have recently been described [24]. In this context, a promising support that has been intensively explored is nanoparticulated silica. Thus, silica can be used either as a carrier for molecular paramagnetic Gd-chelates, as support for Gd_2O_3 nanoparticles or as a coating material for magnetic nanoparticle cores [25–28]. However, direct incorporation of Gd^{3+} ions into the silica matrix to render the material MR active remains as a less explored strategy. Mesoporous silicas can be suitable platforms for MR imaging CA because of their high specific surface areas and large pore volumes, stable 3D structures (forming networks of channels), and excellent biocompatibility. The presence of silanol groups on their surfaces makes them hydrophilic, which is a precondition for any in vivo application. Additionally, the key to designing highly efficient MR imaging CAs is a high accessibility of water to the magnetic centres [28–31]. An approach based on the incorporation of Gd into the silica skeleton would not take up any space in the pores. This strategy would enable accessibility of water towards the paramagnetic centres while allowing that the pore space could be used for loading of drugs or other active molecular agents in theranostic devices [32].

Although from a basic point of view, a reasonable variety of CA appears to be available, clinically "in vivo" barely ten Gd-based T1 CA have been authorized by the FDA and EMA (for intravenous use) [33]. A more restrictive situation takes place for the T2 CA. In fact, the only authorized T2 agent is based on modified iron oxide particles but, in addition, its administration is carried out exclusively orally for gastrointestinal bowel marking [34].

At this point, a fact to highlight is the influence of the magnetic field strength on MR imaging. In practice, the technique is progressively evolving towards more intense fields. Indeed, the MRI instruments typically found in the clinic make use of magnetic fields ranging from 1.5 to 3.0 T. However, the application of MRI scanners working at magnetic fields as high as 9.4 T, firstly employed in preclinical assays (small animals), has been recently reported for human imaging [35]. The increase of the magnetic field intensity leads to greater signal to noise ratios (SNR), higher spatial resolutions and shorter acquisition times. Indeed, these high-field features allow to speak of MR microscopy (MRM). The term MRM specifies the use of ultra-high resolution (<100 μm) MR imaging. This resolution is lower than that of light microscopy (0.25 μm), but much higher than clinical MR (approximately 1 mm in plane resolution) [36]. Therefore, MRM provides a more detailed anatomical picture of tissue than clinical MR: it improves the interpretation of clinical MR images in terms of cell biology processes or tissue patterns [37] and constitutes a promising technique for the non-invasive detection of a great variety of pathologies [38]. However, the time necessary to obtain high-resolution 3D images is noticeably long, typically 10 h. Furthermore, in many ultra-high field equipment, the size of the sample that can be studied is considerably reduced, with the consequent reduction in the signal intensity. To address these problems, most small animal imaging or cell labelling studies are performed by adding MRI CAs. The classical classification in T1 and T2 CAs loses meaning when we are working at ultra-high magnetic fields (≥7 T) because CA MRI performance is clearly magnetic field-dependent.

It is well known that for Gd-based T1 contrast agents, r1 typically decreases with increasing at high fields while r2 is static or increases resulting in an increasing r2/r1 ratio. The T2 effect is the dominant one at the high field (as occurs in MRM) [14,39,40]. It has been published that systems with an excessive gadolinium content may lead to a disproportionate weight of T2 effects, which would have a negative effect on T1 signal [40]. Furthermore, Tseng et al. have pointed out that when the concentration of Gd becomes too high, the effect of T2 relaxation will overcome the effect of T1, thus partially cancelling the T1 signal [41]. Thus, gadolinium-based T2 CAs can be designed for MRM.

There are few reports dealing with Gd incorporation into the framework of nanosized mesoporous silica. Lin et al. [42] reported on Gd-incorporated mesoporous silicas synthesized by using a long-chain surfactant as template. These materials showed proton relaxivities at 9.4 T higher than Gd-DTPA, with longitudinal relaxivity values (r1) ranging from 23.6 to 4.4 $mM^{-1}s^{-1}$ and transverse relaxivity values (r2) from 94.8 to 80.4 $mM^{-1}s^{-1}$ as the Gd loading increases from 1.6% to 6.8 wt%. However, their XRD patterns show a concomitant loss of order towards wormhole like arrays that can restrict the access of water molecules to the metal centres. Shao et al. [43,44] have reported interesting results on two sorts of Gd-doped silica materials. Thus, they described the one-step synthesis of Gd_2O_3@SiO_2 particles displaying an SBA-15-like mesoporous structure [43]. Nevertheless, in these materials, Gd incorporation resulted in an important decrease of the BET surface area (ca. 236.9 m^2g^{-1}) and virtually total loss of textural porosity. On the other hand, they also prepared new Gd_2O_3@MCM-41 materials using the classical procedure for obtaining doped MCM-41solids [44,45]. However, once again, the nanoparticles suffered from the typical drawbacks of low water accessibility and loss of structural features. One alternative approach to synthesize Gd doped silica was used by Liu et al. [46], which replaced the templating surfactant (CTAB) by gadolinium oleate. The resulting Gd-doped samples were amorphous, with low BET surface area (150–200 m^2g^{-1}) and pore volume values. Except for the work by Liu et al., MRI studies were carried out on low fields (in the range of 0.5–3 T), with the study focusing on the influence on r1. In these cases, and working under relatively low magnetic fields, the longitudinal relaxivity values were lower than that corresponding to the commercial Magnevist (r1 = 4.91 $mM^{-1}s^{-1}$). In no case was attention paid to the possibility of enhancing r2 values from compounds containing gadolinium.

Our hypothesis is that the atrane route is a suitable synthesis strategy for maximizing the incorporation of subnanometric homogeneously dispersed Gd clusters in a UVM-7 type bimodal mesoporous silica. The preservation of the hierarchical porous structure could allow the combination of diagnostic and therapeutic activity. These new materials could act as Gd-based T2 CA capable of working efficiently under high magnetic fields, this favouring the progress of the MRM technique.

2. Materials and methods

2.1. Chemicals

All the synthesis reagents were analytically pure and were used as

Table 1
- Preparative parameters and selected physical data for the solids isolated by using the following reagent molar ratio: (2-x) Si: x Gd: 7 TEAH3: 0.5 CTAB: y H_2O: z Ethanol.

										Mesopore[g]		Large pore[g]	
Sample	Si/Gd[a]	Si/Gd[b]	Si/Gd[c] %	Gd[d]/%	y	z	T/days	d_{100}[e]/nm	BET[f]/m^2/g	Size/nm	Vol./cm^3/g	Size/nm	Vol./cm^3/g
UVM-7	–	–	–	–	180	0	1	4.01	1061	3.16	0.95	34.4	1.20
1	100	62	4.0	3.6	180	0	1	4.33	1031	3.15	0.95	57.8	0.83
2	50	42	5.8	5.3	180	0	1	4.51	937	3.00	0.81	51.6	0.51
3	25	22	10.4	11.0	180	0	1	4.85	370	2.95	0.33	35.2	0.09
4	50	26	9.0	8.7	2000	0	1	5.06	991	3.16	0.95	41.4	0.52
5	50	19	11.8	12.2	2880	0	1	4.62	811	3.12	1.01	38.8	1.10
6	50	17	13.0	13.3	1000	200	1	4.00	901	2.54	0.69	32.3	0.91
7	50	13	16.3	16.1	1000	200	10	3.98	884	2.64	0.65	36.1	1.20
8	25	6	29.1	37.5	1000	200	10	–	718	2.58	0.90	69.1	0.31
9	50	19	11.9	12.3	500	300	1	4.00	725	2.45	0.35	29.9	0.76
10	50	11	18.5	20.6	50	450	1	–	458	2.82	0.04	15.5	0.69

[a] Si/Gd nominal molar ratio.
[b] Si/Gd real molar ratio determined by EDX.
[c] Gd content % (wt) determined through EDX assuming a general formula $SiO_2{\cdot}(x/2)Gd_2O_3$ (1/x = Si/Gd).
[d] Gd content % (wt) determined through ICP.
[e] d_{100} spacing from XRD.
[f] Surface area determined by applying the BET model.
[g] Pore sizes and volumes determined by applying the BJH model on the adsorption isotherm branches.

received from Aldrich (tetraethyl orthosilicate [TEOS], 2, 2′,2″-nitrilotriethanol or triethanolamine [$N(CH_2–CH_2–OH)_3$, hereinafter TEAH3], gadolinium and yttrium trichlorides [$GdCl_3{\cdot}6H_2O$, $YCl_3{\cdot}6H_2O$], gadolinium oxide [Gd_2O_3], cetyl-trimethylamonium bromide [CTAB], ethanol (99%), and phosphate-buffered saline (PBS) tablets).

2.2. Synthesis

All solids described here have been prepared through the "atrane route" [47]. This procedure combines using a cationic surfactant as supramolecular template (and, consequently, as porogen after template removal), and atrane-like species (complexes containing ligands derived from TEAH3) as hydrolytic precursors both of Si and Gd. Our objective was to preserve the well-known UVM-7 architecture [48–50] while attaining the maximum gadolinium content homogeneously distributed in the silica network. With this aim, we have performed two series of syntheses. Thus, we have carried out the typical syntheses of M-UVM-7 materials in essentially aqueous media (the molar ratio of the reagents is: (2-x) Si: x Gd: 7 TEAH3: 0.5 CTAB: 180H_2O) [51–53] and, alternatively, we have worked under significantly more diluted conditions in hydro-alcoholic media ((2-x) Si: x Gd: 7 TEAH3: 0.5 CTAB: y H_2O: z EtOH (180 = y ≤ 2880; 0 = z ≤ 450)). In both cases, the nominal Gd content in the mother liquor was varied in the 25 ≤ Si/Gd ≤ 100 range.

In a typical synthesis corresponding to the Si/Gd = 50 mesoporous material (Sample 2 in Table 1), 10.94 mL of TEOS, 25 mL of TEAH3 and 0.36 g of $GdCl_3{\cdot}6H_2O$ were mixed while stirring. The mixture was heated at 140 °C for 5 min until complete dissolution and homogenization (what involves the formation of both Si and Gd atrane-like complexes). The resulting solution was cooled to 120 °C, and 4.56 g of CTAB were added while stirring. When the temperature dropped to 85 °C, 80 mL of water were added. After a few minutes, a white suspension resulted. This mixture was aged at room temperature for 24 h. The resulting mesostructured powder was filtered off, washed with water and ethanol, air-dried and heated at 70 °C for 2 h. Finally, to open the pore system, the surfactant was removed from the as-synthesized solid by calcination at 550 °C during 5 h under static air atmosphere. All the samples in this series were prepared identically (exception made of the relative amounts of the Si and Gd reagents). In the case of the samples prepared in hydroalcoholic media, we have followed the same recipe until achieve the surfactant dissolution. Then, when the temperature decreased to 60 °C, we added the corresponding amounts of ethanol and water. The aging times, under stirring at room temperature, varied from 1 to 10 days. Summarized in Table 1 are the main synthesis variables and physical data referred to both series of samples. Moreover, in order to favour the materials dispersion, the samples can be ultrasonically treated by using a Branson Sonifier 450 instrument equipped with a direct immersion titanium horn operating at 20 kHz, with an intensity of 100 W/cm^2; the sonication treatment was carried out in water, its duration is limited to a 5 min and the system is also kept refrigerated in an ice bath.

Additionally, we have synthesized some silica materials containing simultaneously Gd and Y (see Supplementary Material, Table S1). The magnetic properties of these solids have been studied in order to gain insight on the Gd organization at the subnanoscale. The nominal molar ratio of the reagents was as follows: 1.96 Si: 0.04 (Gd + Y): 7 TEAH3: 0.5 CTAB: 200 EtOH: 1000H_2O, with Y/Gd = 10 and 100. Y was incorporated to the initial reaction mixture jointly with Gd, and the preparative procedure was as described above.

2.3. Materials degradation

We have made a study of the degradation of the materials by using two different concentrations of the solids, namely 0.1 g of solid in 100 mL of PBS (0.1% m/v) and 0.02 g in 200 mL of PBS (0.01% m/v). In both cases, we have used some conditions mimicking biological systems: T = 37 °C and pH = 7.4 (provided by the PBS medium). The PBS solution was prepared by dissolution of one PBS tablet in 200 mL of MiliQ water. This leads to the following concentration of salts: 137 mM NaCl, 2.7 mM KCl and 10 mM phosphate buffer solution. First of all, the samples were sonicated in the respective suspensions for 5 min, and later were incubated in PBS under permanent rotation (150 rpm) by using a magnetic stirrer. In the case of the experiments carried out using relatively high solid proportions, the progress of the degradation process was analysed independently after given reaction times (from 1 h to 7 days), and the solid particles were separated by filtration. The solids were analysed by XRD, TEM, EDX and N_2 adsorption-desorption isotherms. Dealing with the degradation process involving low solid proportions (0.1 g/L), aliquots of ca. 5 mL were taken from the dispersions at given times (from 1 to 24 h). Here, the amount of solid sample was minimum and, consequently, insufficient for any characterization. In all cases, the mother solutions were filtered (0.20 μm syringe filters) in order to remove possible particles in suspension. The solutions were analysed by ICP -MS to detect the solubilized species of Si and Gd.

2.4. Materials characterization

The Si and Gd contents were determined by energy dispersive X-ray spectroscopy (EDX analysis) using a Scanning Electron Microscope (Philips-SEM-XL 30). The Si/Gd molar ratio values averaged from EDX data corresponding to ca. 50 different particles of each sample are summarized in Table 1. Furthermore, the content of Gd has been confirmed by ICP measurements by using an ICP-MS instrument equipped with an Agilent 7900 mass detector. The samples were processed by cold digestion as follows: dried samples were processed in a mixture of HF, HCl, and HNO_3 in a plastic container at room temperature by swirling the contents overnight until complete dissolution. Thereafter a concentrated solution of boric acid is added to the sample. Finally, MiliQ water is added to the mixture to obtain the desired final weight. For electron microscopy analyses, the samples were dispersed in ethanol and placed onto a carbon coated copper microgrid and left to dry before observation. TEM (transmission electron microscopy) and STEM−HAADF (scanning transmission electron microscopy−high-angle annular dark-field) images were acquired with a JEOL-2100 F microscope operated at 200 kV. X-ray powder diffraction (XRD) was carried out using a Bruker D8 Advance diffractometer equipped with a monochromatic CuK_α source operated at 40 kV and 40 mA. Patterns were collected in steps of 0.02° (2θ) over the angular range 1–10.0° (2θ), with an acquisition time of 25 s per step. Additionally, XRD patterns were recorded over a wider angular range, 10–80° (2θ) in order to detect the presence of segregated crystalline phases. Nitrogen adsorption-desorption isotherms were recorded with an automated Micromeritics ASAP2020 instrument. Prior to the adsorption measurements, the samples were outgassed in situ in vacuum (10^{-6} Torr) at 120 °C for 15 h to remove adsorbed gases. XPS spectra were obtained with an Omicron device equipped with an EA-125 hemispheric multichannel electron analyser, and an Mg KKα X-ray monochromatic source with radiation energy of 1253.6 eV. Determination of the grain size has been carried out by using a Malvern Nanosizer ZS instrument. The analysis of the solutions remaining after the degradation steps was performed using an ICP-MS instrument equipped with an Agilent 7900 mass detector. Variable-temperature (2–300 K) direct current (dc) magnetic susceptibility measurements under an applied magnetic field of 0.25 ($T \leq 20$ K) and 5 kOe ($T > 20$ K) were carried out on powdered samples with a Quantum Design SQUID magnetometer. The magnetic data were corrected for the diamagnetism of the silica content of the samples and for the sample holder.

2.5. Water proton relaxivity measurement and MR imaging

The studies of the relaxation times have been performed using a Bruker AVANCE III system equipped with a 5 mm microimaging 1H coil operating at 600 MHz and working under very high magnetic field (14.1 T). The acquisition software used was ParaVision 6.0.1 (Bruker Biospin GmbH, Ettlingen, Germany). Nanoparticles were dispersed in an aqueous solution with different Gd^{3+} ion concentrations; 400 μL of each sample were placed in a 5 mm high-resolution NMR tube, and homogenous dispersion was obtained after sonication for 10 min. All samples were subsequently used for obtaining both relaxation times measurements and MR imaging. The longitudinal T1 and the transverse T2 relaxation times were measured using a multi-slice multi-echo-variable TR (MSMEVTR) sequence. A total of 64 images were acquired at 8 different echo time (TE) values equally spaced from 4.5 to 36 ms and 8 different repetition time (TR) values in the range from 250 to 2500 ms. The parameters used for the measurements were as follows: temperature (T) = 298 K; averages = 2; slices = 5; field of view (FOV) = 10 mm; matrix size = 128 × 128; slice thickness = 2 mm and pixel spacing = 0.078 mm. Relaxation times (T1/T2) for each sample were measured by fitting signal decay curves to a standard model in ParaVision 6.0.1, the operating software for the MRI platform. Subsequently, the inverse of T1 and T2 value versus the gadolinium concentration (mM) plots for each sample were obtained, and the r1 and r2 values (mM^{-1} s^{-1}) were calculated by taking the slope of the line of the best fit. The relaxivity is represented as mM^{-1} s^{-1} ± SD (n = 5). T1-and T2-weighted images were acquired using a rapid acquisition relaxation enhanced sequence (RARE) with a repetition time/echo time (TR/TE) of 1500/9 ms with a number of averages of 8 and TR/TE of 4000/18 ms with 8 averages, respectively. The same geometry was selected for all images with 5 slices equally distributed along the axial direction; the slice thickness was 2 mm, 10 × 10 mm field-of-view and a 256 × 256 image matrix. For the purpose of comparison, same measurements were carried out with commercial CA gadoterate meglumine Dotarem® (Gd-DOTA, Guerbert, France).

2.6. In vitro cell viability assay

The cytotoxicity of the nanoparticles was evaluated using breast cancer MCF-7 cells maintained in Dulbecco's modified Eagle's medium (DMEM, Gibco) containing 10% fetal bovine serum (FBS), L-glutamine (1% v/v), 100 units mL^{-1} penicillin and 100 μg mL^{-1} streptomycin (all GE Healthcare-HyCloneTM) in a humidified atmosphere (37 °C, 5% CO_2). MCF-7 cells were pre-grown in 96 well plates at a density of 5 × 104 cells into each well and allowed to attach for 24 h. Gd-UVM-7 and UVM-7 nanoparticle solutions at different concentrations (0.2, 0.4, 0.6 and 0.8 mg/mL) were prepared in DMEM previously sterilized under UV for 60 min. Before be used, solutions were ultrasound treated in an ultrasonic cleaning unit at a frequency of 37 kHz (60 W power effective) and controlled temperature to 35 °C for 1 h. After 24 h, the medium was replaced by 200 μL of the nanoparticle solution at each concentration and the cells were incubated in 5% CO_2 at 37 °C for 24 h. MCF-7 cells treated only with culture media fixed as a positive control and media only as blank. At the end of the incubation period, the volume in each well was substituted with 200 μL of fresh media and 20 μL of 5 mg/mL sterile filtered 3-(4,5-dimethylthiazol-2-yl)-2,5-diphenyltetrazolium bromide (MTT) solution in PBS. The plate was incubated for additional 4 h at 37 °C, allowing viable cells to metabolically reduce MTT into purple formazan. After addition of 150 μL of dimethyl sulfoxide (DMSO) to each well, the plate was incubated at RT for 10 min on a shaking platform, and the absorbance of each well was measured at λ = 540 nm using a microplate reader (Spectra Max Plus 96, Molecular Devices LLC, CA, USA). The cell viability was calculated after correction for absorbance with the control wells. The date is represented as % Cell viability ± SE as a function of the Gd concentration and % Cell viability = [ODtreated – ODblank/ODcontrol – ODblank] x 100 [54]. All experiments were repeated 3 times for statistical analysis.

3. Results

3.1. Synthesis strategy

The hydrolytic reactivity of Si-alkoxides (like TEOS) and Gd salts is markedly different, and their sol-gel processing normally leads to undesired phase-segregation phenomena [55–57]. In order to avoid this problem, we have used the atrane route, which has already been shown to be useful in the synthesis of bimetallic mesoporous materials [47, 51–53]. This method is based on the idea that, both because of the formation of atrane-like species and due to certain inertness towards hydrolysis in TEAH3-rich media, the rates of the respective reactions of hydrolysis and condensation of different metal or metalloid derivatives result balanced [47]. Then, segregation is not favoured and truly mixed oxides can be obtained without any or minimum phase segregation at the nanoscale. As recently reported, Gd(III) and triethanolamine species can interact showing a stepwise structural variation provided by the progressive deprotonation of the ligand. This leads to initial dimeric entities that can be regarded as the building blocks from which tetramer and hexamer units can be constructed [58–60]. In fact, we have observed that Gd_2O_3, highly insoluble in water, dissolves easily in the

presence of TEAH3. Also, the processing of mixtures of rare-earth elements in rich-TEAH3 media to form mixed oxides was described long time ago [61]. In any case, to slow down the hydrolysis of the Gd species, we have performed the syntheses using hydroalcoholic media (involving ethanol as co-solvent) too.

Regardless of the solvent used (either water or ethanol:water mixtures) and the nominal Si/Gd ratio, in all cases the final materials (Table 1) show a relatively high Gd content. That is, Si/Gd molar ratios determined by EDX (hereinafter real values) are smaller than the stoichiometric values added in the synthesis (hereinafter nominal values). This trend is also confirmed by ICP analysis (Table 1). If we consider that the materials can be described as mixtures of SiO_2 and Gd_2O_3 oxides, it is well known that the solubility of SiO_2 is much greater than that of Gd_2O_3 ($K_{ps} = 1.8 \times 10^{-23}$) [62,63]. Then, the Gd enrichment can be assigned to a partial silica dissolution [62].

In the samples synthesized in aqueous media (Samples 1 to 5), we have observed that the Gd-rich Sample 3 (Si/Gd = 25 nominal molar ratio) results in loss of the UVM-7 structure due to the significant growth of the particle size despite the maintenance of the mesostructured nature (Fig. S1). Conversely, the UVM-7 morphology is preserved (see below) for Samples 1 (Si/Gd = 100 nominal molar ratio) and 2, 4 and 5 (Si/Gd = 50 nominal molar ratio) regardless their real (final) Gd content. The progressive enrichment in Gd with the water amount in the media (Samples 2, 4 and 5) must be associated to the silica solubility [62].

Dealing with the materials synthesized in ethanol: water media (Samples 6 to 10), we have observed (see below) that as the ethanol proportion increases, the order in the porous structure diminishes. The typical (100) signal of the XRD patterns tends to disappear and the BET surface area diminish in a marked way (Table 1). In fact, Sample 10 losses the UVM-7 organization (Fig. S2). The progressive difficulty in stabilizing the mesostructure in the presence of relatively large proportions of ethanol must be related to a mismatch in the self-assembling processes of the inorganic oligomers and the CTAB surfactant micelles. It is well known that surfactants of this type are highly soluble in ethanol [64]. Indeed, the cmc value of the CTAB surfactant grows as the relative amount of ethanol increases [65]. For molar ratios Si/EtOH $\leq$100, the proportion of stabilized micelles decreases, making it difficult to establish a suitable fit with the inorganic counterparts through S^+I^- interactions. Thus, the optimum proportion of the molar ratio of the reagents (in order to get our objectives) is as follows: 2 (Si + Gd): 7 TEAH3: 0.5 CTAB: 200 EtOH: 1000H_2O.

Finally, the last variable we have explored in this series is the aging time. With respect to the chemical composition of the final materials, the resulting real Si/Gd molar ratios are very similar after aging times of 1 or 10 days at room temperature. There are also no significant differences regarding the organization at mesoscopic scale. However, we have observed that the final materials are more easily dispersible in aqueous media as the aging time increases (see below). This aspect is important when considering biomedical applications. Then, in accordance with our objectives (preserve the UVM-7 architecture while attaining the maximum gadolinium content in the silica network), the data in Table 1 suggest that the optimum molar ratio of the reagents is around 1.96 Si: 0.04 Gd: 7 TEAH3: 0.5 CTAB: 1000H_2O: 200 EtOH, what corresponds to Samples 6 and 7.

3.2. Chemical and mesostructural characterization

We have used EDX and ICP to assess both the stoichiometry and the chemical homogeneity of the samples, given that an important objective of our work is to favour also a good dispersion of Gd into the inorganic silica-based walls of the resulting materials. The real Si/Gd molar ratio are summarized in Table 1. EDX data show that all the reported materials are chemically homogeneous at the spot area scale (ca. 1 μm). As commented above, in the entire compositional (nominal) range studied ($\infty \geq$ Si/Gd $\geq$ 25), the value of the Si/Gd molar ratio in the final solid decreases with respect to that in the mother solution, what indicates an

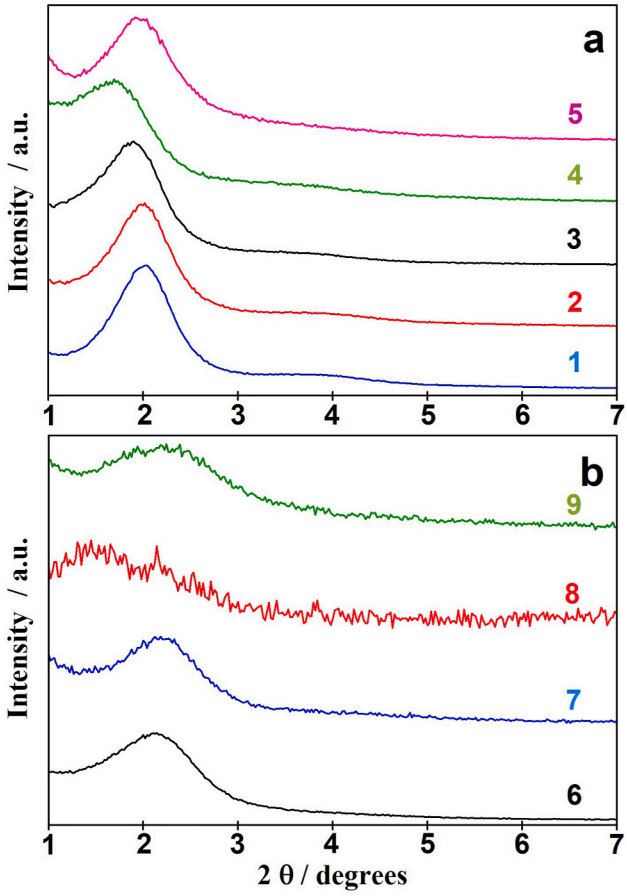

Fig. 1. Low-angle XRD patterns of samples synthesized (**a**) without ethanol (Samples **1** to **5**) and (**b**) with ethanol (Samples **6** to **9**) [in the reaction medium].

enrichment in Gd independently of the reaction medium. The values of Gd% (wt) determined by ICP are in reasonable agreement with those estimated by EDX with the exception of the two materials richest in Gd (Samples 8 and 10) that are far from the UVM-7 type architecture. These samples, with less order and porosity and a more massive nature (see below), show a higher Gd content determined by ICP than those determined by EDX. In any case, and regardless the final morphology, this fact indicates a preferential incorporation of Gd into the final silica network due to the gadolinium oxide insolubility. Excluding incipient impregnation, our "one pot" procedure has allowed us to insert Gd amounts in the silica net higher than those previously reported in the literature, reaching 11.8% (by weight, with respect to silica determined from EDX) in aqueous medium (Sample 5; Si/Gd = 19) and 16.3% in hydroalcoholic medium (Sample 7; Si/Gd = 13), while maintaining the UVM-7 architecture. Similar values have been determined by ICP: 12.2 and 16.1% for Samples 5 and 7, respectively. Specifically, regarding "one pot" strategies, we have managed to significantly increase the maximum value reported by Lin et al. (6.8%), who also used $GdCl_3{\cdot}6H_2O$ as Gd source in aqueous medium [42]. This achievement is a consequence of the harmonization among the reaction rates of the hydrolytic processes involving the Si and Gd species that provides the atrane route.

On the other hand, the complete absence of XRD peaks in the high-angle domain (Fig. S3) allows us to discard the existence of ordered large domains of Gd_2O_3, Gd-silicates or any other crystalline phase (although the existence of related nanodomains smaller than 5 nm cannot be rejected) [66]. Hence, the final solids can be considered as monophasic products, and segregation of crystalline Gd_2O_3 can be practically discarded even for the samples having the highest Gd

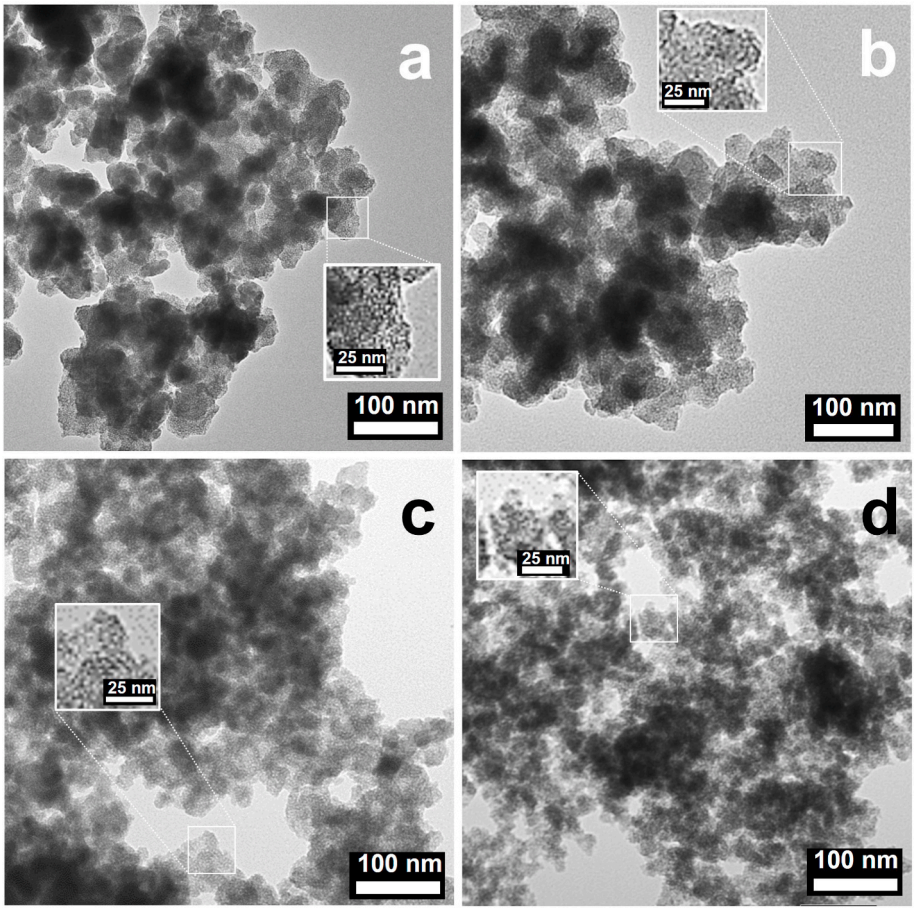

Fig. 2. Representative TEM images of Gd-UVM-7 materials. (**a**) Sample **2**, (**b**) Sample **4**, (**c**) Sample **6** and (**d**) Sample **7**.

contents (even though, probably, the formation of Gd_2O_3-like clusters should progress with the Gd content).

Exception made of the solid synthesized with the higher ethanol proportion (Sample 10), all the remaining materials display XRD patterns with diffraction peaks in the low-angle regime (Fig. 1). This indicates the stabilization of self-assembled mesostructures. In the case of the mesoporous solids synthesized in the absence of ethanol (Samples 1–5), the low-angle region of the XRD patterns displays, apart from the intense peak at low 2θ values (associated with the (100) reflection if a basic hexagonal cell is assumed), a broad signal or shoulder of relatively low intensity that can be indexed to the overlapped (110) and (200) reflections of the typical hexagonal cell. The observation of this last unresolved broad signal is characteristic of a MCM-41-like disordered hexagonal (intra-particle) mesopore topology. In the case of the samples isolated in hydroalcoholic media (Samples 6–9), although the (100) intense peaks at low angle values also appear in the corresponding XRD patterns, their fwhm (full width at half maximum) values increase when compared to those of the peaks corresponding to Samples 1–5. Moreover, the shoulder assigned to the (110) and (200) overlapped reflections practically disappears, which suggests a relative loss of order of the intra-particle mesopore array [48–50]. Also, as the ethanol proportion increases, the intensity of the (100) signal decreases, which is obvious in the case of Sample 9 (and culminates with its disappearance in the pattern of Sample 10 (Fig. S2)).

On the other hand, when we start from a relatively high nominal Gd content (Si/Gd = 25, Sample 8), the use of a hydro-alcoholic medium does not allow the recovery of the UVM-7 morphology. Then, as occurs for the samples isolated in aqueous medium, the UVM-7 architecture is lost for Sample 8 (Fig. S4). Then, as occurs with the samples isolated in aqueous medium, the UVM-7 architecture is lost for Sample 8 according to TEM images (Fig. S4) and XRD data (the intensity of the (100) signal practically disappears) (Fig. 1b). The pronounced loss of UVM-7 morphology leads to solids with greater aggregation and a more massive nature. In these cases, and also due to the greater insolubility of the Gd species, it could be reside the origin of the discrepancies between the ICP and EDX measurements: the former inform us of the average composition of the material while the EDX values inform us of the Gd content closest to the surface. In the case of Gd-UVM-7 materials made up of nanoparticles, the differences can be expected to be minimal or null, according to our experimental results (Table 1).

The d_{100} spacing peak and the lattice parameter value slowly decrease with the Gd content (Samples 1 to 3, synthesized in the absence of ethanol). This cell expansion probably is due to the replacement of Si atoms with Gd ones. On the other hand, for an identical Si/Gd = 50 nominal molar ratio (and similar real Gd contents in the 13 to 19 Si/Gd range), there is not an appraisable effect of the ethanol proportion and the reaction time on the d_{100} spacing value. Indeed, a very similar value around 4 nm is measured for Samples 6, 7 and 9. What is appreciated is a decrease in the spacing value with the incorporation of ethanol into the reaction medium, from ca. 4.3–4.8 (Samples 1, 2 and 3) to 4 nm (Samples 6, 7 and 9). This evolution suggests either a decrease in the thickness of the inorganic wall or the size of the mesopore.

The TEM images in Fig. 2 clearly show that the UVM-7-like architecture is preserved for real Si/Gd molar ratios higher that ca. 13, this value implying a high hetero-element content. In this real compositional range ($\infty \geq$ Si/Gd ≥ 13), all the solids present a continuous nanometric array constructed from aggregates of mesoporous nanoparticles.

Although certain pseudosphericity and nanoparticle size homogeneity is lost when compared to the pure silica material due to Gd incorporation, we can consider that the UVM-7 architecture is

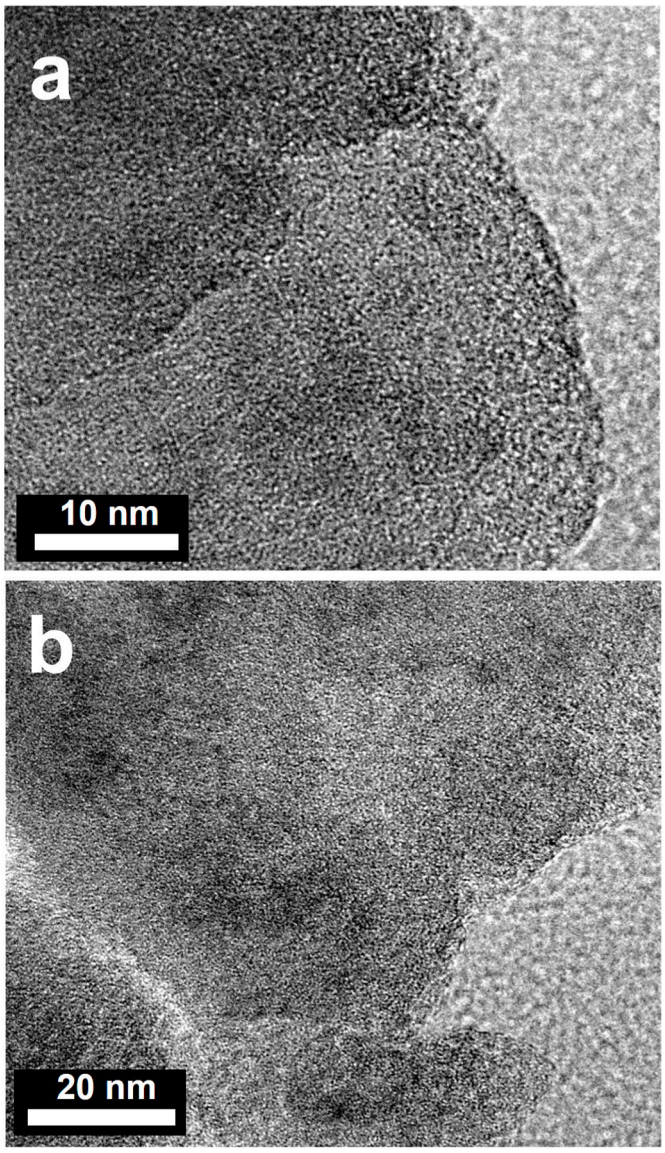

Fig. 3. HRTEM images of (**a**) Sample **2** and (**b**) Sample **7**.

preserved. This array includes two different pore systems: (1) the first one is due to the porogen effect of the surfactant micelles, which generates the small intra-particle regular mesopores organized in a disordered hexagonal arrangement, and (2) the second one consists of large cage-like inter-particle voids appearing as consequence of the primary nanoparticle aggregation.

Qualitatively, there is no difference among the TEM images of the solids prepared with or without ethanol. However, two details should be mentioned: 1) the average size of the primary particles is smaller for the samples prepared in hydroalcoholic media (ca. 40–60 nm for samples 1, 2, 4, 5 and ca. 20–30 nm for samples 6, 7, 9), and 2) the presence of ethanol in the reaction medium leads to a relatively minor inter-particle aggregation. Both trends are in accordance with the synthesis conditions. Indeed, it can be expected that the hydrolysis and condensation processes will be favoured as the water content increases. Dark spots that could be attributed to Gd_2O_3 nanodomains are not observed in any case (even in HRTEM images (Fig. 3)).

In the same way, the STEM-HAADF images (Figs. 4 and 5) show the absence of bright spots associated to Gd-rich domains. A homogeneous and continuous bright is observed throughout the entire mass of the samples both in the case of samples isolated in water (Fig. 4a, d and 4g) and those prepared in water: ethanol media (Fig. 5a and d). In addition, the dispersion of Si and Gd has been studied by spherical aberration (Cs) corrected scanning transmission electron microscopy high-angle annular dark field (STEM-HAADF). The mappings of selected samples are included in Figs. 4 and 5. Rich-Gd zones are not detected. There is a regular and homogeneous distribution of both elements. The effect of the Gd content is clearly appreciated in Fig. 4 (b, c, e, f, h, i), which includes the Si and Gd distribution in Samples 1, 2 and 4. The homogeneous and regular dispersion of both elements does not seem to be affected by changes in their relative concentrations. As shown in Fig. 5 (b, c, e, f), such a good dispersion of the elements is also attained for samples isolated in water: ethanol media (Samples 7 and 9) having a similar Gd content. At this point, all data unambiguously confirm the absence of phase segregation even at the nanoscale. Then, all suggests a truly regular nanodispersion of Gd in the net, either replacing Si atoms in isolated sites or in the form of small Gd-containing oligomers.

The materials porosity was further characterized by N_2 adsorption-desorption isotherms (Fig. 6, Table 1). The bimodal pore system typical of nanoparticulated UVM-7 silicas is maintained in the Gd-UVM-7 materials whose real Si/Gd molar ratios are comprised in the ranges $\infty \geq Si/Gd \geq 26$ (solids synthesized in the absence of ethanol) or $\infty \geq Si/Gd \geq 13$ (solids synthesized in presence of ethanol). The first adsorption step, at intermediate partial pressures ($0.3 < P/P_0 < 0.5$), is due to the capillary condensation of N_2 inside the intra-nanoparticle mesopores. The second step, at a high relative pressure ($P/P_0 > 0.8$), corresponds to the filling of the large inter-particle cage-like pores. In the series of solids prepared in the absence of ethanol, all the textural parameters (BET surface area, pore sizes and pore volumes) decreases as the Gd content increases. However, while this variation is not very great between Samples 1 and 2, in the case of Sample 3 all the parameters decrease abruptly, and, what is more relevant, the textural porosity disappears.

Perhaps the main difference between the two families of materials is the BJH mesopore sizes. These range from 2.45 to 2.64 nm and from 2.95 to 3.16 nm for the samples isolated with and without ethanol as co-solvent, respectively. This intra-particle mesopore size variation is probably the origin of the d_{100} decrease detected from the XRD patterns, and can be due to changes in the nature of the micelles caused by the solvent. This effect was previously described for pure UVM-7 silicas [48].

Due to the interest of these materials as MR CA, the degree of aggregation and the mean grain size of the particle-clusters have been studied using DLS. As it is well known, the UVM-7 architecture implies a significant inter-particle condensation degree [48–53]. The effect of ultrasound protocols on the dispersion level has been analysed (Fig. S5). When subjected to a simply treatment in an ultrasounds bath during some minutes, the original UVM-7 silica shows wide particle size distributions in the micrometric range. By applying more vigorous treatments (by using a Branson Sonifier 450 instrument), a significant grain size decrease until ca. 350 nm can be achieved. Similar results are obtained in the case of Samples processed in water rich media (without ethanol). However, we have observed that, by using strictly the same ultrasounds treatment, the disaggregation of samples aged in rich ethanol media can be significantly improved up to average grain sizes around 100 nm. The solid after sonication post-treatment continues to retain its bimodal pore system. On the other hand, ICP-MS measurements of Si concentration in supernatant solution justly after sonication are very low (ca. 1–2 ppm), indicating that a negligible dissolution of the solid occurs during the post-treatment. Then, we can conclude that the effect of the ethanol in the reaction medium is not limited to favouring the incorporation of Gd to the network, but also contributes to improving the dispersibility of the final material.

3.3. *Characterization of the Gd organization in the materials*

The direct current (dc) magnetic properties of the synthesized materials are compared with those of Gd_2O_3 bulk material in Fig. 7. Our objective at this point is to understand how the Gd atoms are dispersed

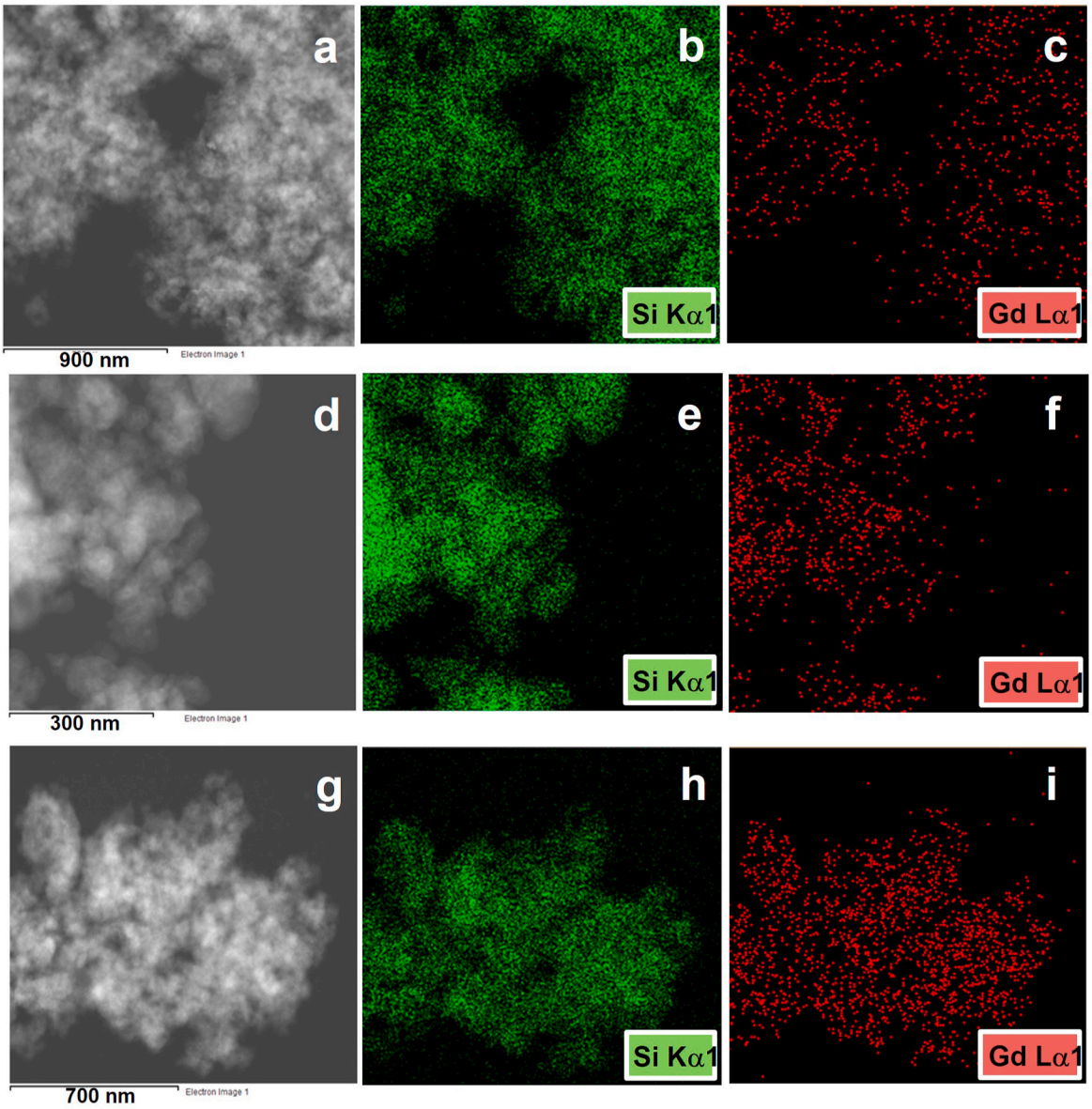

Fig. 4. STEM-HAADF images and mapping showing the Si and Gd distribution of (**a**, **b**, **c**) Sample **1**, (**d**, **e**, **f**) Sample **2** and (**h**, **i**, **j**) Sample **4**.

throughout the silica-based walls. In order to compare with the Gd_2O_3 reference sample, we have selected the two Gd-richest materials: Samples 7 and 8 (which preserve the intra-particle mesopore system according to XRD and porosimetry data), although, as commented above, the large particle size in the case of Sample 8 does not allow considering it as UVM-7 type. The χ_mT vs. T plots (χ_m being the dc magnetic susceptibility per g of sample and T the absolute temperature) for Samples 7 and 8 are qualitatively similar. χ_mT remains constant from room temperature until around 20 K, with χ_mT values of 0.62×10^{-2} and 2.31×10^{-2} $cm^3\ g^{-1}$ K (for Samples 7 and 8, respectively), and then it decreases slowly down to 0.31×10^{-2} and 1.17×10^{-2} $cm^3\ g^{-1}$ K at 2 K (Fig. 7a). In contrast, χ_mT continuously decreases upon cooling for the Gd_2O_3 bulk material, with χ_mT values varying from 4.31×10^{-2} $cm^3\ g^{-1}$ K at room temperature down to 0.47×10^{-2} $cm^3\ g^{-1}$ K at 2 K, although there is no long-range antiferromagnetic order, as revealed by the absence of a maximum in the χ_m vs. T plot (data not shown). These smaller deviations from the Curie law for the Samples 7 and 8 relative to the bulk material support the absence of Gd_2O_3 particles of nanometric size grown during the aggregation process. Hence, the $1/\chi_m$ vs. T plots for the for Samples 7 and 8 show a typical linear Curie-Weiss law behaviour with a similar negative value of the Weiss temperature around −2 K, estimated from the interception with the T axis, which is diverse and rather smaller (in absolute value) than that of ca. −18 K for the bulk Gd_2O_3 material (Fig. 7b) [67].

The molar magnetic susceptibility of the bulk material was first analysed through the Curie-Weiss law (eq. (1)), where g is the isotropic Landé factor of the GdIII ion (S = 7/2) and θ is the Weiss temperature, while N is the Avogadro number, β is the Bohr magneton, and k_B is the Boltzman constant. The least-squares fit of the experimental data lead to g = 2.056(2) and θ = −17.9(1) K with $F = 1.8 \times 10^{-6}$ (F is the agreement factor defined as $F = \sum[(\chi_MT)_{exp} - (\chi_MT)_{calcd}]^2/\sum[(\chi_MT)_{exp}]^2$). The mass magnetic susceptibility of the Samples 7 and 8 was then analysed through a modified Curie-Weiss law (eq. (2)), which includes the α variable that takes into account the Gd mass loading for each sample (expressed as g of Gd per g of sample), where MW(Gd) is the gadolinium atomic weight [MW(Gd) = 157.25]. The least-squares fits of the experimental data, with a fixed g value taken from the fit of the experimental data of the bulk material (g = 2.056), lead to θ = 2.02(1)/–2.04 (1) K (Sample 7/Sample 8) and α = 0.1185(1)/0.4384(1) (Sample 7/Sample 8) with $F = 0.1/0.3 \times 10^{-6}$ (Sample 7/Sample 8). The

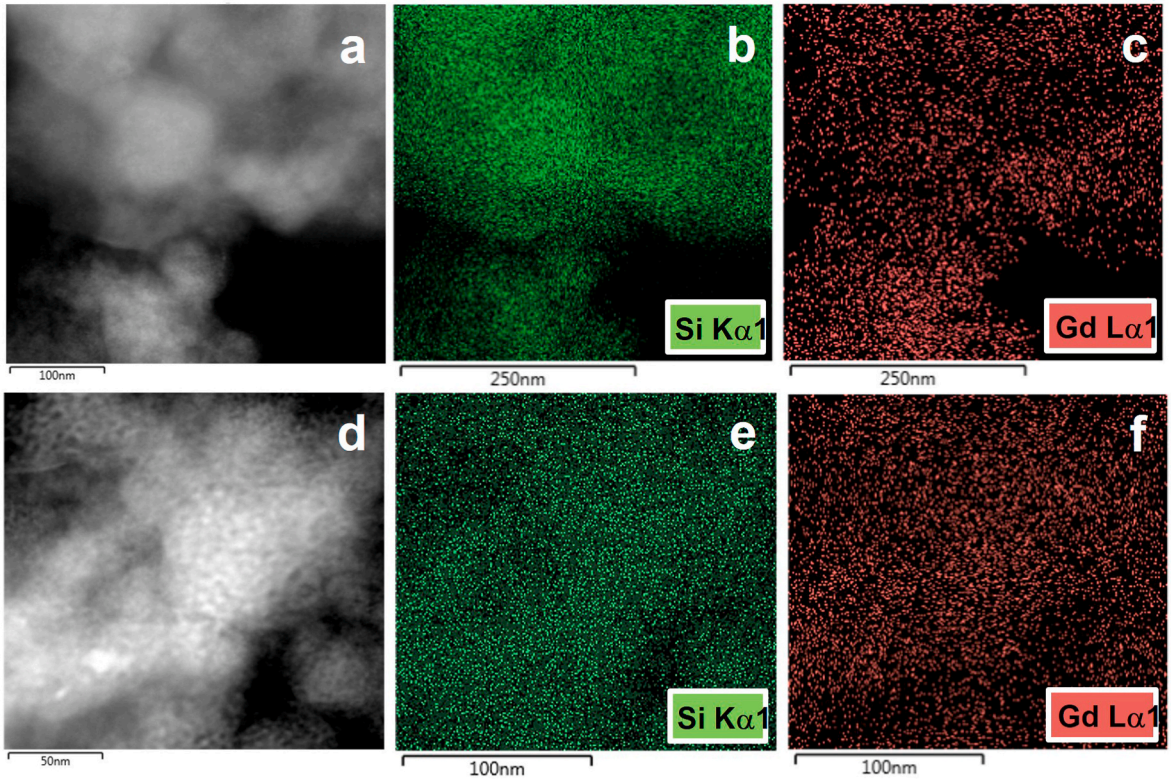

Fig. 5. STEM-HAADF images and mapping showing the Si and Gd distribution of (**a**, **b**, **c**) Sample **7** and (**d**, **e**, **f**) Sample **9**.

theoretical curves reproduce rather well the experimental data in all the temperature range (solid lines in Fig. 7a and b). Within a simple molecular field model, the Weiss temperature can be expressed by eq. (3) [68,69], where j is the effective magnetic coupling parameter and z is the number of next neighbours around each Gd^{III} ion, so that –zj = 2.37 (1) cm^{-1} for the bulk material while –zj = 0.267(1)/0.270(1) cm^{-1} (Sample 7/Sample 8).

$$\chi_M = (N\,\beta^2\,g^2/3k_B)S(S+1)/(T-\Theta) \quad (1)$$

$$\chi_m = [\alpha/MW(Gd)](N\,\beta^2\,g^2/3k_B)S(S+1)/(T-\Theta) \quad (2)$$

$$\Theta = (zj/3k_B)S(S+1) \quad (3)$$

This almost ten-fold decrease of the magnetic coupling between the Gd^{III} ions across the oxo bridges from the bulk material to the corresponding Samples 7 and 8 is likely associated to the formation of small oligonuclear oxo-bridged Gd_n clusters of finite size, not reaching the Gd_2O_3 nanoparticle size domain, as reported earlier for the aggregation of magnetic gadolinium(III) oxide nanoparticles under different conditions. The calculated values of the Gd mass loading amount of 12% and 43% for Samples 7 and 8, respectively, roughly agree with those calculated from ICP (16.1 and 37.5% for Samples 7 and 8, respectively). In the case of the EDX measurements, the agreement is maintained for Sample 7 but a greater discrepancy occurs for Sample 8. Thus, as previously discussed, for a $SiO_2{\cdot}(n/2)Gd_2O_3$ general formula with 1/x = Si/Gd = 13 and 6 for Samples 7 and 8 [α = xMW(Gd)/MW($SiO_2{\cdot}$(x/2) Gd_2O_3) = 157.25x/(60 + 181.25x)] α values of 16.3 and 29.1% are determined, respectively. In this respect, the similarity between the calculated –zj values for the two gadolinium-silica nanocomposites, regardless of the Gd mass loading amount (and even for samples with different morphology), is consistent with a similar average nuclearity of the small oligonuclear oxo-bridged Gd_n clusters and they only differ in their concentration.

On the other hand, the effect of the paramagnetic metal dilution on the dc magnetic properties has also been investigated in the corresponding mixed Gd-Y-UVM-7 nano-composites. In fact, the diamagnetic rare earth yttrium(III) ion is commonly used in solid dilution experiments of paramagnetic gadolinium(III)-based materials because Y^{3+} and Gd^{3+} ions have similar ionic radii due to the well-known lanthanide contraction phenomenon. Hence, the χ_MT vs. T plots for the diluted Gd10/Y90 and Gd1/Y99 samples are qualitatively similar. χ_MT remains constant from room temperature until around 5 K, with χ_MT values of 3.04/0.41 × 10^{-4} cm^3 g^{-1} K (Gd10Y90/Gd1Y99), and then it slightly decreases down to 2.52/0.34 × 10^{-4} cm^3 g^{-1} K (Gd10Y90/Gd1Y99) at 2 K (inset of Fig. 7a). These very small deviations from the Curie law for the diluted Gd10/Y90 and Gd1/Y99 samples relative to the parent Gd-UVM-7 samples are as expected because of the weaker next nearest-neighbour antiferromagnetic interactions (when compared to the stronger nearest-neighbour antiferromagnetic interactions across the oxo bridges within the Gd_n clusters) between the magnetically isotropic Gd^{III} ions (S = 7/2) through the diamagnetic Y^{III} ions (S = 0) within the oxo-bridged $(Gd_yY_{1-y})_n$ clusters,. In fact, the $1/\chi_m$ vs. T plots for the diluted Gd10Y90 and Gd1Y99 samples show a linear Curie-Weiss law behaviour with a very small (if not negligible) negative value of the Weiss temperature around −0.5 K, which is characteristic of almost magnetically isolated Gd^{III} ions (inset of Fig. 7b).

The least-squares fits of the experimental mass magnetic susceptibility data for the diluted Gd10Y90 and Gd1Y99 samples through the modified Curie-Weiss law (eq. (2), with g = 2.056), lead to θ = −0.42 (1)/0.47(1) K (Gd10Y90/Gd1Y99) and α = 0.00587(1)/0.000790(1) (Gd10Y90/Gd1Y99) with F = 0.4/0.2 × 10^{-10} (Gd10Y90/Gd1Y99), so that –zj = 0.056(1)/0.062(1) cm^{-1} (Gd10Y90/Gd1Y99). The theoretical curves reproduce perfectly well the experimental data in the low-temperature region (solid lines in the insets of Fig. 7a and b). Indeed, the calculated values of the Gd mass loading amount of 0.587 and 0.079% for Gd10Y90 and Gd1Y99, respectively, agree rather well with those expected upon 1:10 and 1:100 Gd/Y dilution. Otherwise, the similarity between the calculated –zj values for the two mixed Gd-Y-UVM-7 nanocomposites, regardless of the paramagnetic metal dilution

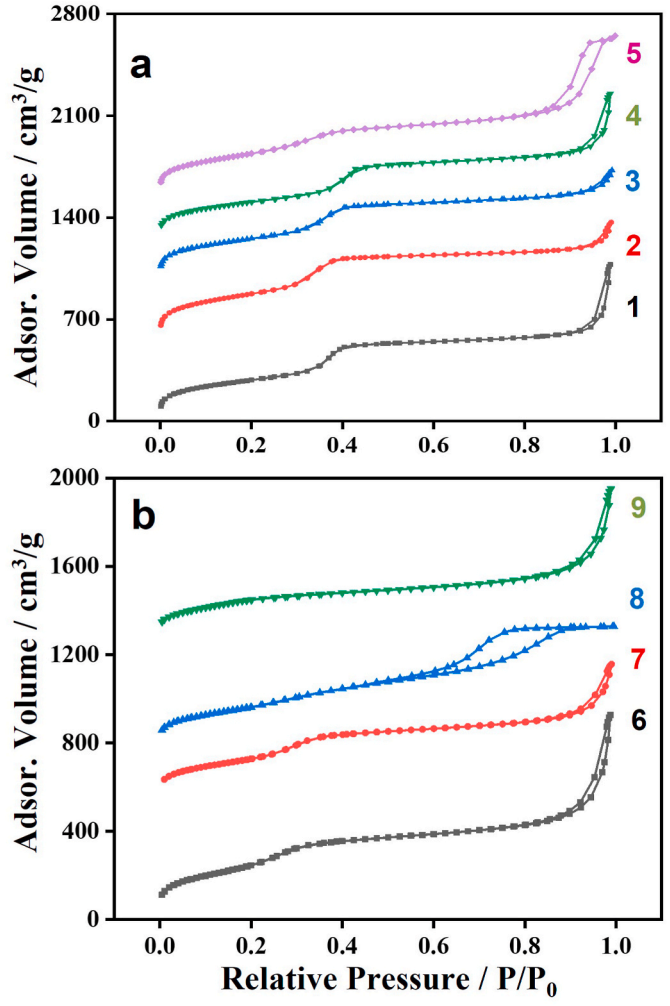

Fig. 6. N_2 adsorption-desorption isotherms of samples synthesized (**a**) without ethanol (Samples **1** to **5**) and (**b**) with ethanol (Samples **6** to **9**) [in the reaction medium].

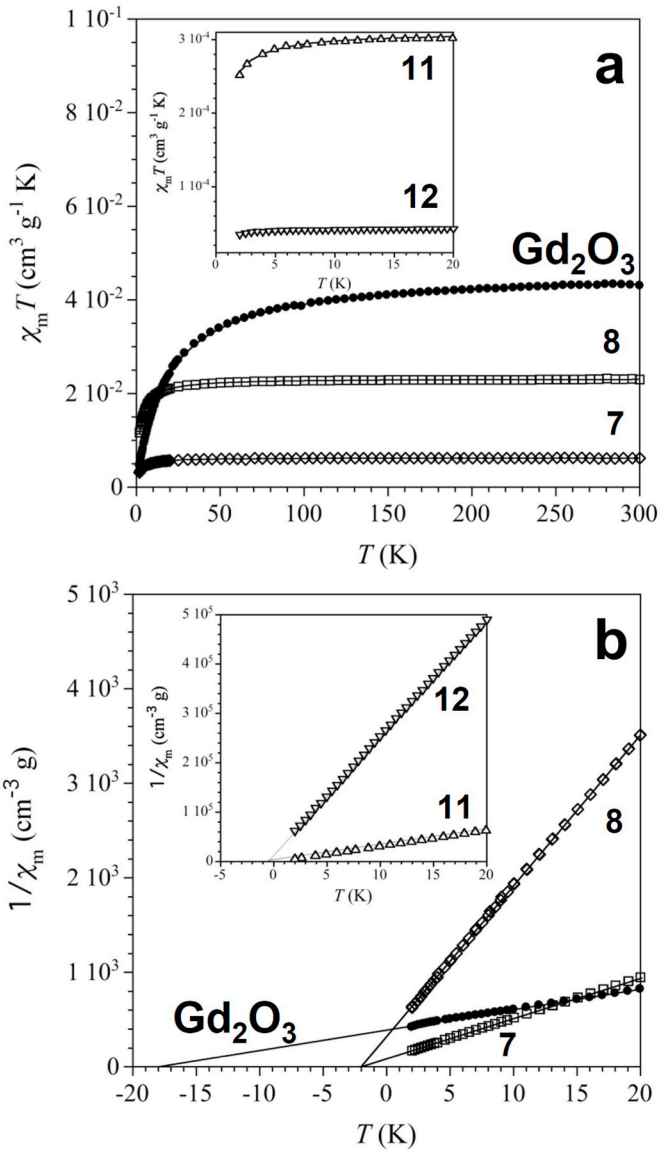

Fig. 7. Temperature dependences of $\chi_m T$ (a) and $1/\chi_m$ (b) for Samples **7** and **8** compared with those for the bulk material Gd_2O_3. The inset shows the temperature dependences of $\chi_m T$ **(a)** and $1/\chi_m$ **(b)** for the gadolinium(III)-yttrium (III)/UVM-7 nanocomposites, Samples **11** and **12**. The solid lines are the best-fit curves (see text).

amount, is consistent with almost magnetically isolated Gd^{III} ions. Hence, the observed very small Curie law deviations can be explained by the ligand-field zero-field splitting (zfs) effects associated with the very weak, but non-negligible, local magnetic anisotropy of the Gd^{III} ions. Then a maximum rough limit of the Gd_n oxo clusters nuclearity can be established that corresponds to n = 10. This maximum value is in accordance with the previously commented nuclearity for the Gd-atrane complexes.

On the other hand, when compared the XPS spectra of selected Gd-UVM-7 samples with the pure silica parent and Gd_2O_3 as references (Fig. S6), it is evident the absence of large Gd_2O_3 nanodomains [70]. The Gd $3d_{5/2}$ peak is shifted towards low binding energy values as the Gd content decreases while the Si 2p XPS peak remains practically un-changed and centred at 103.4 eV. The presence of shoulder in the XPS O 1s band could be likely attributed to Gd-*O*-Si bridges.

3.4. Magnetic resonance imaging under high magnetic fields

Having into mind the objective of developing novel Gd doped silica nanoparticles as MR CA, the proton longitudinal and transverse relaxivities, r1 and r2, were determined at 14.1 T for Sample 7. MRI relaxivity as a function of Gd(III) concentration is shown in Fig. 11. Gadolinium-silica nanoparticles presented a r1 value of 1.24 $mM^{-1}s^{-1}$ and r2 value of 120.4 $mM^{-1}s^{-1}$ at room temperature. Longitudinal relaxivity is lower than a commercial standard Gd-DOTA contrast agent Dotarem® with a r1 value of 2.89 $mM^{-1}s^{-1}$ also measured at 14.1 T. In contrast, our Gd–Si nanoparticles presented 29 times higher transversal relaxivity value than that corresponding to the commercial CA (r2 = 4.12 $mM^{-1}s^{-1}$). Most interestingly, the r2 relaxivity values of Sample 7 are also higher than those described for other Gd-doped mesoporous silicas [42,46]. When comparing the relaxivity of the synthesized Gd-UVM-7 mesoporous material (Sample 7) with an ordered porous silicate material as reported by Lin et al. [42] (6.8 wt% Gd and measured at 9 T), the selected nanoparticulate Gd-UVM-7 presented 1.5 times higher r2 value, probably due to our higher Gd content (which is achieved thanks to the use of the atrane method).

The apparently low longitudinal relaxivity, despite the high gadolinium content, may be understood as the consequence of two major factors: a large payload of Gd^{3+} centres incorporated into the mesoporous silica matrix, and the use of a very high magnetic field (14.1 T) for the material characterization [39,40]. The T1 relaxivity of molecular Gd^{3+} compounds typically decrease as the magnetic field increases [71]. The effect of the magnetic field on relaxation is more marked for slowly

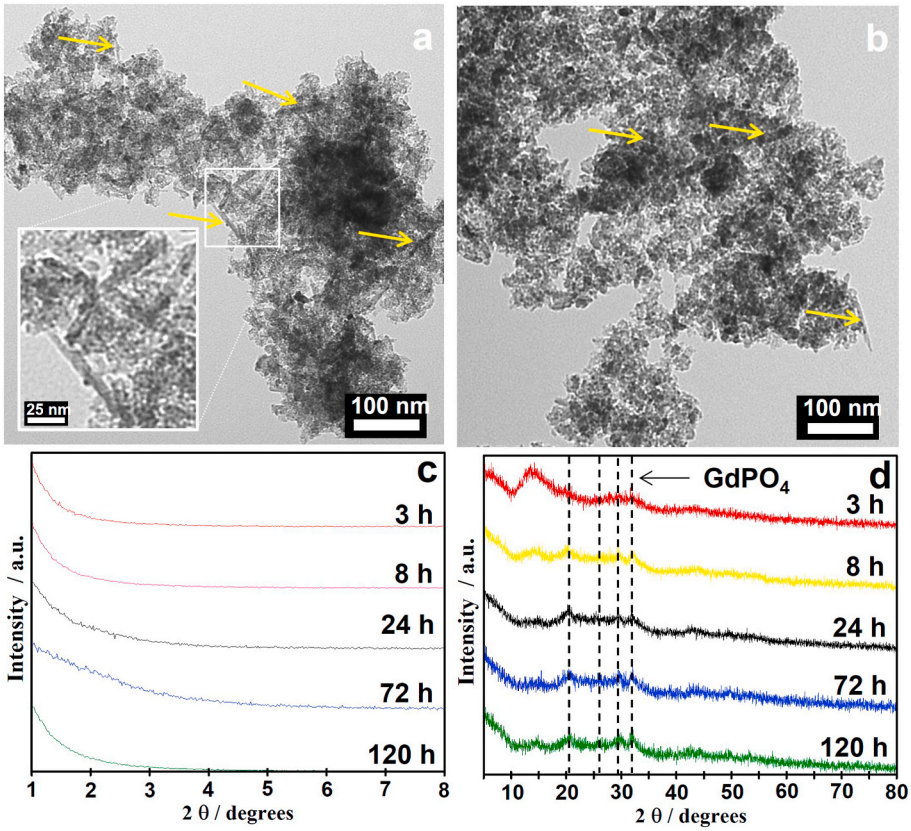

Fig. 8. TEM images of Sample **7** after degradation in PBS during (**a**) 8 h and (**b**) 120 h. The inset in Fig. 8a and the yellow arrows show the presence of $GdPO_4$ elongated crystals. Graphics (**c**) and (**d**) show the evolution with degradation time of the low-angle and high-angle XRD patterns, respectively. The vertical dotted lines in figure (**d**) correspond to the position of the principal XRD peaks for the $GdPO_4$ (according to the JCPDS card number 320386). (For interpretation of the references to colour in this figure legend, the reader is referred to the Web version of this article.)

rotating molecules than for rapidly rotating molecules [72]. Thus, small molecules such as Gd-DOTA show a restricted decrease in r1 with higher magnetic fields. On the contrary, a greater decrease in r1 can be expected for the less mobile gadolinium centres inserted in siliceous particles. On the other hand, the transverse relaxivity was also found to depend on the concentration of gadolinium content. In a detailed work by Liu et al. observed that the transverse relaxivity reached an optimum value at 1.8 atomic percent gadolinium doping for their disordered gadolinosilicate [46]. Further increase of gadolinium doping resulted in a decrease in transverse relaxivity [46]. It has also been described a field-dependent behaviour in the r2 values. The r2 values are static or increase in the presence of higher field strength [72,73]. Yeh et al. [74] established that a field-dependent transversal relaxivity intensify may be explained by the chemical exchange model as proposed by Brook et al. [75]. The chemical exchange model is restricted to weakly magnetized particles in strong fields, for which magnetic susceptibility result associated with a magnetized centre is prevailing.

In short, the high content of Gd, its homogeneous distribution in the form of small oligomers, the easy accessibility of the water molecules through the bimodal porous system and especially the use of very high magnetic fields, are parameters consistent with the low r1 and relatively high r2 relaxivity values achieved.

3.5. Nanomaterial behaviour in biological fluids and citotoxicity

Degradation and clearance are the final steps of nanomedicines after actuation. Usually we think in mesoporous silicas as stable and robust supports. However, reality is far from it. Without an external particle protection, which is normally provided by an adequate functionalization using organic species, the silica degradation and dissolution occurs, especially under circumneutral and basic pH conditions. Silica is unstable in water and dissolves to give silicic acid species ($Si(OH)_4$ is the dominant species at low con-centration), which have an excellent bioavailability and are excreted through the urine. The biocompatibility of silica and its degradation by-products accounts for their generally recognized safety. We have performed two series of degradation experiments in PBS medium (see Experimental section). In the first one, we have used a relatively high concentration of the material (1 g of material/L of solution) in order to brake the dissolution rate (simply by working upon the saturation limit). This long-term experiment allows us to analyse in detail how the silica degradation starts. On the other hand, the second short-term series has been carried out under dilution conditions similar to those occurring in biological systems (0.1 g of material/L of solution). We have selected the Sample 7 for the degradation study due to their magnetic properties and excellent dispersibility.

Although the typical aggregation of primary particles is preserved (TEM) even after 5 days, the hexagonal intra-particle mesostructure, detected through XRD, rapidly disappears (after 3 h) (Fig. 8). As time progresses, TEM images show a certain reduction in the particle size together with a lower definition of the mesopore white spots. Both factors contribute to the loss of the low-angle XRD signals. The evolution of the N_2 adsorption-desorption isotherms allows to monitor the degradation process in a more quantitative way. Thus, it can be appreciated a gradual decrease in both the BET surface area and the intra-particle BJH pore volume (Table S2).

Apparently, a certain degradation/dissolution also occurs in the inner walls. This lead to an increases of the BJH intraparticle mesopore size and a less homogeneous pore size distribution. In fact, the maximum in the pore distribution analysis disappears for degradation times higher than 8 h. Parallel to the degradation of the mesostructure, broad signals of low intensity begin to appear in the high-angle XRD patterns after only 3 h (Fig. 8d). These new peaks can be unambiguously attributed to a $GdPO_4$ crystalline phase (PBS acts as source of phosphate). This fact is in accordance with the EDX data, which show a quick increase in the gadolinium content (from Si/Gd = 13 to Si/Gd in the 8–9 range), and the detection of P as new element in our solid samples (Table S2). This can

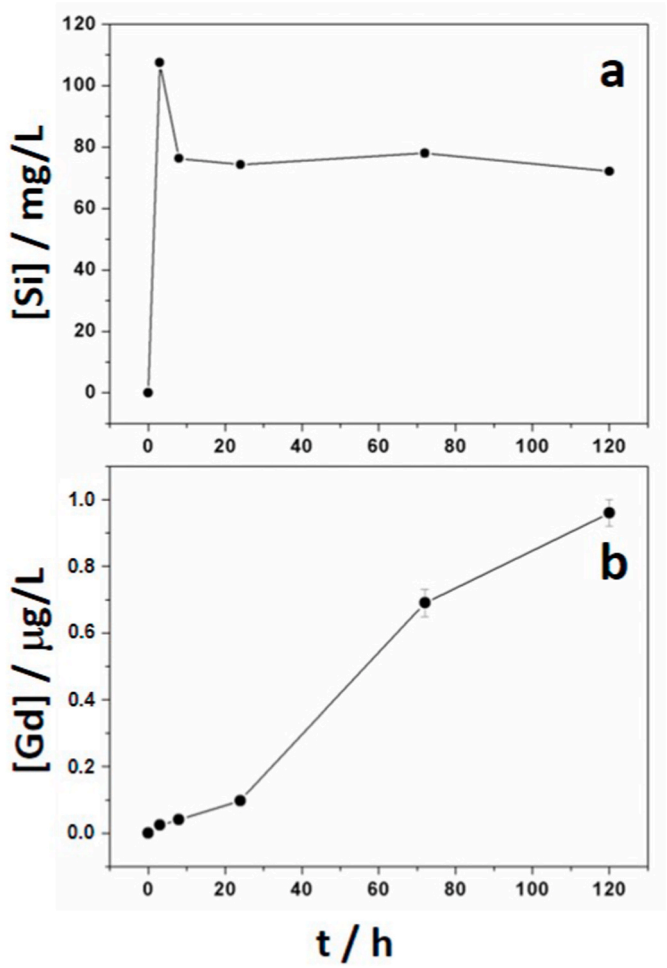

Fig. 9. Evolution of the concentrations in the supernatant solutions of (**a**) silicon and (**b**) gadolinium over time during the degradation experiment carried out under conditions of higher concentration.

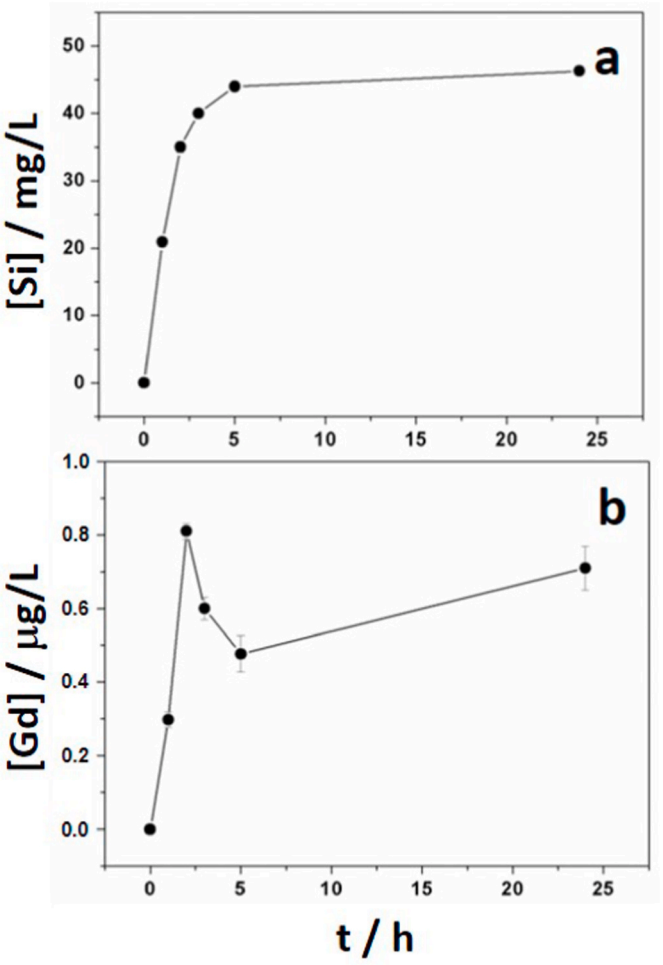

Fig. 10. Evolution of the concentrations in the supernatant solutions of (**a**) silicon and (**b**) gadolinium over time during the degradation experiment carried out under diluted conditions.

be related to the easy partial dissolution of the silica and the favoured precipitation of $GdPO_4$. The evolution with time of the Si and Gd concentrations in the supernatant solutions is in good agreement with these observations (Fig. 9).

Indeed, occurs a rapid increase of the Si concentration in the solution during the first hours (up to 107 mg/L), and then it stabilizes at a lower value (ca. 75 mg/L). The peak is very close to the maximum silica solubility in water at neutral pH and ambient temperature: 120 mg/L [62] (with small deviations from this value in the T range between 20 and 50 °C [76] and circumneutral pH values [77]). Yet, this saturation level may be altered by the presence of solubilizing agents in the solution as for example the PBS. In fact, similar values to the here described, slightly higher than 100 mg/L, has been reported working in PBS at pH = 7.4 and 37 °C [78]. The evolution of solubility vs time in our case suggests a partial reprecipitation of silica oligomers in the period of time between 3 and 8 h. On the contrary, the variation of the Gd concentration over time present a sigmoidal tendency, with a low dissolution rate during the first hours, and practically negligible after 3 h of incubation.

Very likely, it is necessary certain initial silica elimination before an appreciable amount of Gd can be detected. Then, the aging of the sample should favour some silica coating (from the Si-olygomers) of the whole material with the subsequent trapping of the more insoluble Gd-rich domains. Moreover, according to the XRD results, a proportion of the Gd precipitates with phosphate anions. In fact, TEM images show, together with the partially degraded Gd-UVM-7 aggregates, the formation of elongated nanocrystals (with dimensions of ca. 5 × 15 nm) that probably correspond to the $GdPO_4$ (Fig. 8a and b). These reduced dimensions are in agreement with the low intensity and the large fwhm values observed in the XRD patterns.

The short-time experiment, with conditions similar to the application of the material in biological media, shows that the silica degradation is practically completed after incubations of ca. 5 h (Fig. 10). This quick silica dissolution favours a massive leaching of the Gd-based oligomers. Then, the [Gd] in solution quickly increases before its precipitation as $GdPO_4$, which qualitatively explain the curve tendency. While the final concentration of Si in solution is very different for both series (ca. 75 and 45 ppm for experiments performed under high and low concentration conditions, respectively), this is similar in the case of Gd (in the 0.7–0.9 µg/L range), which seems be controlled by the formation of highly insoluble phosphate. Then, when working under concentrations mimicking those that take place in biological systems, the final degradation products are solubilized silica oligomers and $GdPO_4$ nanoparticles.

Finally, in order to validate the cytocompatibility of the nanomaterials in a biological environment, cell viability was assessed 24 h after incubation of MCF-7 cells with UVM-7 and Gd-UVM-7 (Sample 7) nanoparticles at a range of different particle concentrations (200, 400, 600, 800 µg mL^{-1}). MTT assay showed (Fig. 12) cell viability was always more than 95% of the untreated cells control even at maximum particle concentration. The results did not indicate significant changes in the cell viability for both of the tested materials at the studied concentrations, indicating no evidence of that both UVM-7 and Gd-UVM7 nanoparticles

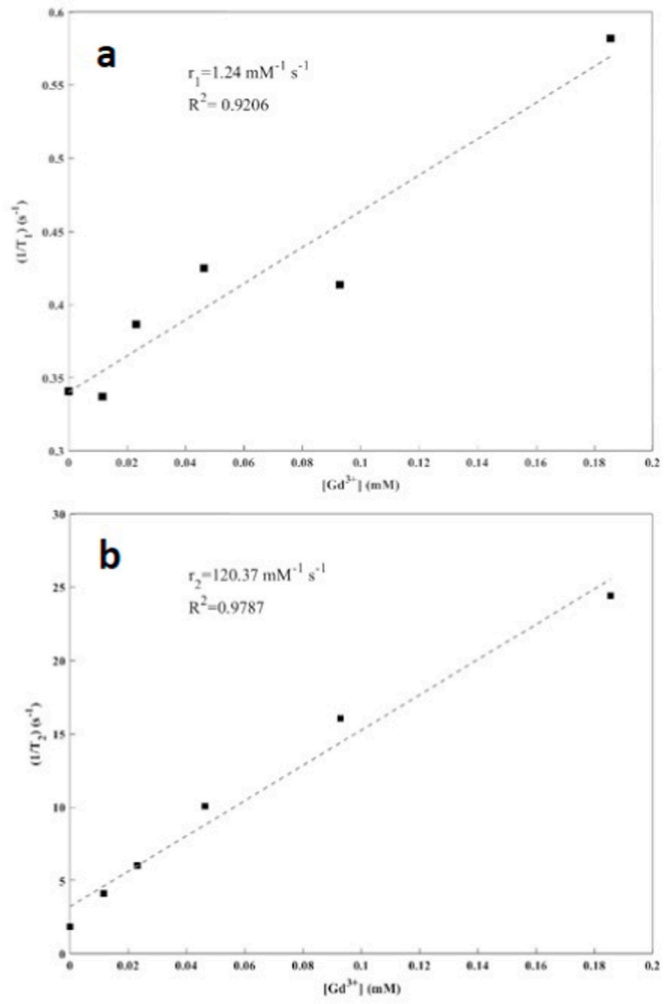

Fig. 11. The proton relaxivities, (**a**) r1 and (**b**) r2, determined at 600 MHz at room temperature for Sample **7** aqueous suspensions measured at 14.1 T.

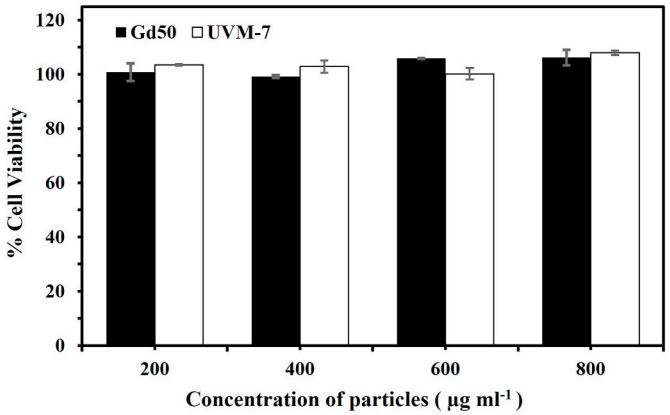

Fig. 12. Cell viability values estimated by the MTT assay, which was performed by treating MCF-7 cells with different concentrations of the Sample **7** (black) and UVM-7 (white) nanoparticulated silicas. The error bars were calculated based on three parallel measurements.

were cytotoxics. The good biocompatibility must be attributed to chemical inertness, low toxicity and reduced leakage of free toxic Gd^{3+} ions from the silica matrix to the cell medium together with the formation of $GdPO_4$. Recent works remark the low toxicity of colloidal suspensions of $GdPO_4$ [79]. Thus, M. Yon et al. [80] suggest that the use of inorganic nanoparticles instead of Gd complexes strengthens the stability of Gd within the formed nanoparticles and thus limits the release of Gd^{3+} ions.

4. Conclusions

Our preparative strategy, based on the atrane route, has allowed to isolate potential theranostic materials based on bimodal porous silicas with the highest gadolinium content, as far as we known, reported up to date in the bibliography. This method prevents the phase segregation even at the nanoscale. Then, according to HRTEM, STEM-HAADF and EDX, the Gd sites result extremely well dispersed along the inorganic silica-based walls. Additionally, the dispersion at molecular level has been proved through magnetic measurements. In fact, a maximum nuclearity of ca. 10 Gd/cluster is calculated. We studied the material degradation in PBS solution at 37 °C. After a few hours, the solid evolves until dissolution of the silica in the form of small olygomers and the Gd-counterpart generate small $GdPO_4$ nanoparticles. No toxicity has been detected in vitro. The high Gd concentration together the coating of the Gd-clusters by silica and the use of ultrahigh magnetic fields confers these Gd-UVM-7 solids good characteristics to act as CA in MRM for diagnostic with a remarkable increase of the T2 relaxivity when compared to others CA, including the molecules in use in medical practice. That enhanced T2 contrast effect and the water-permeable nature of its 3D nanosized matrix, makes Gd-UVM-7 material an excellent candidate for clinical imaging in a multitude of medical applications and as a member of a new-generation MRI CAs where very few dedicated agents have been reported.

CRediT authorship contribution statement

M. Dolores Garrido: Conceptualization, Formal analysis, Methodology, Investigation. **Nuria Puchol:** Formal analysis, Investigation, Methodology. **Jamal El Haskouri:** Writing – original draft, Methodology, Investigation, Formal analysis, Writing – review & editing. **Juan Francisco Sánchez-Royo:** Formal analysis, Investigation, Methodology. **José Vicente Folgado:** Methodology, Investigation, Formal analysis. **Vannina Gonzalez Marrachelli:** Formal analysis, Investigation, Methodology. **Itziar Pérez Terol:** Writing – original draft. **José Vicente Ros-Lis:** Conceptualization, Funding acquisition, Project administration, Supervision, Validation, Writing – original draft, Writing – review & editing. **M. Dolores Marcos:** Investigation, Formal analysis, Methodology. **Rafael Ruíz:** Formal analysis, Investigation, Methodology. **Aurelio Beltrán:** Writing – review & editing, Writing – original draft, Validation. **José Manuel Morales:** Formal analysis, Investigation, Methodology, Validation. **Pedro Amorós:** Conceptualization, Project administration, Funding acquisition, Validation, Writing – original draft, Writing – review & editing, Supervision.

Declaration of competing interest

The authors declare that they have no known competing financial interests or personal relationships that could have appeared to influence the work reported in this paper.

Acknowledgments

This research was carried out thanks to the grant RTI2018-100910-B-C44 funded by MCIN/AEI/10.13039/501100011033 (Spain) and by "ERDF A way of making Europe" (European Union). We also thank the Conselleria d'Educació, Investigació, Cultura i Esport of Generalitat Valenciana (Spain), grant number GV/2018/111. We appreciate the technical support of the SCSIE of the Universitat de València and the Electron Microscopy Service of the Universidad Politécnica de Valencia.

Appendix A. Supplementary data

Supplementary data to this article can be found online at https://doi.org/10.1016/j.micromeso.2022.111863.

References

[1] P. Mansfield, Snapshot magnetic resonance imaging, Angew. Chem. Int. Ed. 43 (2004) 5456–5464, https://doi.org/10.1002/anie.200460078.

[2] P. Caravan, J.J. Ellison, T.J. McMurry, R.B. Lauffer, Gadolinium(III) chelates as MRI contrast agents: structure, dynamics, and applications, Chem. Rev. 99 (1999) 2293–2352, https://doi.org/10.1021/cr980440x.

[3] A market summary report for MRI is available at: http://www.imvinfo.com/.

[4] R.B. Lauffer, Paramagnetic metal complexes as water proton relaxation agents for NMR imaging: theory and design, Chem. Rev. 87 (1987) 901–927, https://doi.org/10.1021/cr00081a003.

[5] A.S. Merbach, L. Helm, E. Toth, The Chemistry of Contrast Agents in Medical Magnetic Resonance Imaging, Wiley, New York, 2013, https://doi.org/10.1002/9781118503652.

[6] H.B. Na, I.C. Song, T. Hyeon, Inorganic nanoparticles for MRI contrast agents, Adv. Mater. 21 (2009) 2133–2148, https://doi.org/10.1002/adma.200802366.

[7] H.B. Na, T. Hyeon, Nanostructured T1 MRI contrast agents, J. Mater. Chem. 19 (2009) 6267–6273, https://doi.org/10.1039/B902685A.

[8] S. Dumas, V. Jacques, W.C. Sun, J.S. Troughton, J.T. Welch, J.M. Chasse, H. Schmitt-Willich, P. Caravan, High relaxivity magnetic resonance imaging contrast agents Part 1. Impact of single donor atom substitution on relaxivity of serum albumin-bound gadolinium complexes, Invest. Radiol. 45 (2010) 600–612, https://doi.org/10.1097/RLI.0b013e3181ee5a9e.

[9] T.J. Meade, A.K. Taylor, S.R. Bull, New magnetic resonance contrast agents as biochemical reporters, Curr. Opin. Neurobiol. 13 (2003) 597–602, https://doi.org/10.1016/j.conb.2003.09.009.

[10] J. Wahsner, E.M. Gale, A. Rodríguez-Rodríguez, P. Caravan, Chemistry of MRI contrast agents: current challenges and new frontiers, Chem. Rev. 119 2 (2019) 957–1057, https://doi.org/10.1021/acs.chemrev.8b00363.

[11] H. Kato, Y. Kanazawa, M. Okumura, A. Taninaka, T. Yokawa, H. Shinohara, Lanthanoid endohedral metallofullerenols for MRI contrast agents, J. Am. Chem. Soc. 125 (2003) 4391–4397, https://doi.org/10.1021/ja027555+.

[12] B. Sitharaman, L.J. Wilson, Gadofullerenes and gadonanotubes: a new paradigm for high-performance magnetic resonance imaging contrast agent probes, J. Biomed. Nanotechnol. 3 (2007) 342–352, https://doi.org/10.1166/jbn.2007.043.

[13] P. Caravan, Strategies for increasing the sensitivity of gadolinium based MRI contrast agents, Chem. Soc. Rev. 35 (2006) 512–523, https://doi.org/10.1039/B510982P.

[14] M.A. Bruckman, X. Yu, N.F. Steinmetz, Engineering Gd-loaded nanoparticles to enhance MRI sensitivity via T1 shortening, Nanotechnology 24 (2013) 462001, https://doi.org/10.1088/0957-4484/24/46/462001.

[15] J. Pellico, C.M. Ellis, J.J. Davis, Nanoparticle-based paramagnetic contrast agents for magnetic resonance imaging, Contrast Media Mol. Imaging (2019) 13, https://doi.org/10.1155/2019/1845637. Article ID 1845637.

[16] W. Zhang, L. Liu, H. Chen, K. Hu, I. Delahunty, S. Gao, J. Xie, Surface impact on nanoparticle-based magnetic resonance imaging contrast agents, Theranostics 8 (2018) 2521–2548, https://doi.org/10.7150/thno.23789.

[17] J.L. Bridot, A.C. Faure, S. Laurent, C. Rivière, C. Billotey, B. Hiba, M. Janier, V. Josserand, J.L. Coll, L.V. Elst, R. Muller, S. Roux, P. Perriat, O. Tillement, Hybrid gadolinium oxide nanoparticles: multimodal contrast agents for in vivo imaging, J. Am. Chem. Soc. 129 (2007) 5076–5084, https://doi.org/10.1021/ja068356j.

[18] J.Y. Park, M.J. Baek, E.S. Choi, S. Woo, J.H. Kim, T.J. Kim, J.C. Jung, K.S. Chae, Y. Chang, G.H. Lee, Paramagnetic ultrasmall gadolinium oxide nanoparticles as advanced T1 MRI contrast agent: account for large longitudinal relaxivity, optimal particle diameter, and in VivoT1 MR images, ACS Nano 3 (2009) 3663–3669, https://doi.org/10.1021/nn900761s.

[19] Y.S. Yoon, B.I. lee, K.S. Lee, H. Heo, J.H. Lee, S.H. Byeon, I.S. Lee, Fabrication of a silica sphere with fluorescent and MR contrasting $GdPO_4$ nanoparticles from layered gadolinium hydroxide, Chem. Commun. (J. Chem. Soc. Sect. D) 46 (2010) 3654–3656, https://doi.org/10.1039/B927570C.

[20] M.F. Dumont, C. Baligand, Y. Li, E.S. Knowles, M.W. Meisel, G.A. Walter, D. R. Talham, DNA surface modified gadolinium phosphate nanoparticles as MRI contrast agents, Bioconjugate Chem. 23 (2012) 951–957, https://doi.org/10.1021/bc200553h.

[21] J. Fang, P. Chandrasekharan, X.L. Liu, Y. Yang, Y.B. Lv, C.T. Yang, J. Ding, Manipulating the surface coating of ultra-small Gd_2O_3 nanoparticles for improved T1-weighted MR imaging, Biomaterials 35 (2014) 1636–1642, https://doi.org/10.1016/j.biomaterials.2013.11.032.

[22] S.M. Siribbal, J. Schläfer, S. Ilyas, Z. Hu, K. Uvdal, M. Valldor, S. Mathur, Air-stable gadolinium precursors for the facile microwave-assisted synthesis of Gd_2O_3 nanocontrast agents for magnetic resonance imaging, Cryst. Growth Des. 18 (2018) 633–641, https://doi.org/10.1021/acs.cgd.7b00787.

[23] J. Yin, D. Chen, Y. Zhang, C. Li, L. Liu, Y. Shao, MRI relaxivity enhancement of gadolinium oxide nanoshells with a controllable shell thickness, Phys. Chem. Chem. Phys. 20 (2018) 10038–10047, https://doi.org/10.1039/C8CP00611C.

[24] A.L. Popov, M.A. Abakumov, I.V. Savintseva, A.M. Ermakov, N.R. Popova, O. S. Ivanova, D.D. Kolmanovich, A.E. Baranchikov, V.K. Ivanov, Biocompatible dextran-coated gadolinium-doped cerium oxide nanoparticles as MRI contrast agents with high T1 relaxivity and selective cytotoxicity to cancer cells, J. Mater. Chem. B 9 (2021) 6586–8559, https://doi.org/10.1039/D1TB01147B.

[25] K.M.M. Taylor, J.S. Kim, W.J. Rieter, H. An, W. Lin, W. Lin, Mesoporous silica nanospheres as highly efficient MRI contrast agents, J. Am. Chem. Soc. 130 (2008) 2154–2155, https://doi.org/10.1021/ja710193c.

[26] K.M.L. Taylor-Pashow, J.D. Rocca, W. Lin, Mesoporous silica nanoparticles with Co-condensed gadolinium chelates for multimodal imaging, Nanomaterials 2 (2012) 1–14, https://doi.org/10.3390/nano2010001.

[27] M.A. Ballem, F. Söderlind, P. Nordblad, P. Käll, M. Odén, Growth of Gd_2O_3 nanoparticles inside mesoporous silica frameworks, Microporous Mesoporous Mater. 168 (2013) 221–224, https://doi.org/10.1016/j.micromeso.2012.10.009.

[28] R. Guillet-Nicolas, J.-L. Bridot, Y. Seo, M.-A. Fortin, F. Kleitz, Enhanced relaxometric properties of MRI "positive" contrast agents confined in three-dimensional cubic mesoporous silica nanoparticles, Adv. Funct. Mater. 21 (2011) 4653–4662, https://doi.org/10.1002/adfm.201101766.

[29] A. Cabrera-García, A. Vidal-Moya, Á. Bernabeu, J. Pacheco-Torres, E. Checa-Chavarria, E. Fernández, P. Botella, Gd-Si oxide nanoparticles as contrast agents in magnetic resonance imaging, Nanomaterials 6 (2016) 109, https://doi.org/10.3390/nano6060109.

[30] W.J. Rieter, J.S. Kim, K.M.L. Taylor, H. An, W. Lin, T. Tarrant, W. Lin, Hybrid silica nanoparticles for multimodal imaging, Angew. Chem. Int. Ed. 46 (2007) 3680–3682, https://doi.org/10.1002/anie.200604738.

[31] J.S. Kim, W.J. Rieter, K.M.L. Taylor, H. An, W. Lin, W. Lin, Mesoporous silica nanospheres as highly efficient MRI contrast agents, J. Am. Chem. Soc. 129 (2007) 8962–8963, https://doi.org/10.1021/ja710193c.

[32] M.S. Usman, M.Z. Hussein, S. Fakurazi, F.F.A. Saad, Gadolinium-based layered double hydroxide and graphene oxide nano-carriers for magnetic resonance imaging and drug delivery, Chem. Cent. J. 11 (2017) 47, https://doi.org/10.1186/s13065-017-0275-3.

[33] Molecular Imaging and Contrast Agent Database (MICAD), National Center for Biotechnology Information (US), Bethesda (MD), 2004–2013. Available from: http://www.ncbi.nlm.nih.gov/books/NBK5330/.

[34] J. Estelrich, J.M.J. Sánchez-Martín, M.A. Busquets, Nanoparticles in magnetic resonance imaging: from simple to dual contrast agents, Int. J. Nanomed. 10 (2015) 1727–1741, https://doi.org/10.2147/IJN.S76501.

[35] T. Vaughan, L. DelaBarre, C. Snyder, J. Tian, C. Akgun, D. Shrivastava, W. Liu, C. Olson, G. Adriany, J. Strupp, P. Andersen, A. Gopinath, A.F. Van de Moortele, M. Garwood, K. Ugurbil, Improved gradient-echo 3D magnetic resonance imaging using pseudo-echoes created by frequency-swept pulses, Magn. Reson. Med. 56 (2006) 1274–1282, https://doi.org/10.1002/mrm.20821.

[36] A. Badea, G.A. Johnson, Modern trends in imaging VII: magnetic resonance microscopy, Anal. Cell Pathol. 35 (2012) 205–227, https://doi.org/10.3233/ACP-2011-0050.

[37] A. Gonzalez-Segura, J.M. Morales, J.M. Gonzalez-Darder, R. Cardona-Marsal, C. Lopez-Gines, M. Cerda-Nicolas, D. Monleon, Magnetic resonance microscopy at 14 tesla and correlative histopathology of human brain tumor tissue, PLoS One 6 11 (2011), e27442, https://doi.org/10.1371/journal.pone.0027442.

[38] I. Perez-Terol, C. Rios-Navarro, E. deDios, J.M. Morales, J. Gavara, N. Perez-Sole, A. Diaz, G. Minana, R. Segura-Sabater, C. Bonanad, A. Bayés-Genis, O. Husser, J. V. Monmeneu, M.P. Lopez-Lereu, J. Nunez, F.J. Chorro, A. Ruiz-Sauri, V. Bodi, D. Monleon, Magnetic resonance microscopy and correlative histopathology of the infarcted heart, Sci. Rep. 9 (2019), 20017, https://doi.org/10.1038/s41598-019-56436-5.

[39] P. Caravan, C.T. Farrar, L. Frullano, R. Uppal, Influence of molecular parameters and increasing magnetic field strength on relaxivity of gadolinium- and manganese-based T1 contrast agents, Contrast Media Mol. Imaging 4 (2009) 89–100, https://doi.org/10.1002/cmmi.267.

[40] V.S. Marangoni, O. Neumann, L. Henderson, C.C. Kaffes, H. Zhang, R. Zhang, S. Bishnoi, C. Ayala-Orozco, V. Zucolotto, J.A. Bankson, P. Nordlander, N.J. Halas, Enhancing T1 magnetic resonance imaging contrast with internalized gadolinium (III) in a multilayer nanoparticle, Proc. Natl. Acad. Sci. Unit. States Am. 114 (2017) 6960–6965, https://doi.org/10.1073/pnas.1701944114.

[41] C.L. Tseng, I.L. Shih, L. Stobinski, F.H. Lin, Gadolinium hexanedione nanoparticles for stem cell labeling and tracking via magnetic resonance imaging, Biomaterials 31 (2010) 5427–5435, https://doi.org/10.1016/j.biomaterials.2010.03.049.

[42] Y.S. Lin, Y. Hung, J.K. Su, R. Lee, C. Chang, M.L. Lin, C.Y. Mou, Gadolinium(III)-Incorporated nanosized mesoporous silica as potential magnetic resonance imaging contrast agents, Phys. Chem. B 108 (2004) 15608–15611, https://doi.org/10.1021/jp047829a.

[43] Y.Z. Shao, L.Z. Liu, S.Q. Song, R.H. Cao, H. Liu, C.Y. Cui, X. Li, M.J. Bie, L. Li, A novel one-step synthesis of Gd3+-incorporated mesoporous SiO2 nanoparticles for use as an efficient MRI contrast agent, Contrast Media Mol. Imaging 6 (2011) 110–118, https://doi.org/10.1002/cmmi.412.

[44] S. Li, H. Liu, L. Li, N.Q. Luo, R.H. Cao, D.H. Chen, Y.Z. Shao, Mesoporous silica nanoparticles encapsulating Gd_2O_3 as a highly efficient magnetic resonance imaging contrast agent, Appl. Phys. Lett. 98 (2011), 093704, https://doi.org/10.1063/1.3560451.

[45] Y. Shao, X. Tian, W. Hu, Y. Zhang, H. Liu, H. He, Y. Shen, F. Xie, L. Li, The properties of Gd_2O_3-assembled silica nanocomposite targeted nanoprobes and their application in MRI, Biomaterials 33 (2012) 6438–6446, https://doi.org/10.1016/j.biomaterials.2012.05.065.

[46] G. Liu, N.M.K. Tse, M.R. Hill, D.F. Kennedy, C.J. Drummond, Disordered mesoporous gadolinosilicate nanoparticles prepared using gadolinium based ionic liquid emulsions: potential as magnetic resonance imaging contrast agents, Aust. J. Chem. 64 (2011) 617–624, https://doi.org/10.1071/CH11064.

[47] S. Cabrera, J. El Haskouri, C. Guillem, J. Latorre, A. Beltrán, D. Beltrán, M. D. Marcos, P. Amorós, Generalised syntheses of ordered mesoporous oxides: the atrane route, Solid State Sci. 2 (2000) 405–420, https://doi.org/10.1016/S1293-2558(00)00152-7.

[48] J. El Haskouri, D. Ortiz de Zárate, C. Guillem, J. Latorre, M. Caldés, A. Beltrán, D. Beltrán, A.B. Descalzo, G. Rodríguez-López, R. Martínez-Máñez, M.D. Marcos, P. Amorós, Silica-based powders and monoliths with bimodal pore systems, Chem. Commun. (2002) 330–331, https://doi.org/10.1039/B110883B.

[49] J. El Haskouri, J.M. Morales, D. Ortiz de Zárate, L. Fernández, J. Latorre, C. Guillem, A. Beltrán, D. Beltrán, P. Amorós, Nanoparticulated silicas with bimodal porosity: chemical control of the pore sizes, Inorg. Chem. 47 (18) (2008) 8267–8277, https://doi.org/10.1021/ic800893a.

[50] M. Pérez-Cabero, A.B. Hungría, J.M. Morales, M. Tortajada, D. Ramón, A. Moragues, J. El Haskouri, A. Beltrán, D. Beltrán, P. Amorós, Interconnected mesopores and high accessibility in UVM-7-like silicas, J. Nanoparticle Res. 14 (2012) 1045, https://doi.org/10.1007/s11051-012-1045-8.

[51] D. Ortiz de Zárate, A. Gómez-Moratalla, C. Guillem, A. Beltrán, J. Latorre, D. Beltrán, P. Amorós, High-zirconium-content nano-sized bimodal mesoporous silicas, Eur. J. Inorg. Chem. 13 (2006) 2572–2581, https://doi.org/10.1002/ejic.200501140.

[52] L.J. Huerta, P. Amoros, D. Beltran, V. Cortes, Selective oxidative activation of isobutane on a novel vanadium-substituted bimodal mesoporous oxide V-UVM-7, Catal. Today 117 (2006) 180–186, https://doi.org/10.1016/j.cattod.2006.05.016.

[53] J. El Haskouri, D. Ortiz de Zárate, F. Pérez-Pla, A. Cervilla, C. Guillem, J. Latorre, M.D. Marcos, A. Beltrán, D. Beltrán, P. Amorós, Improving epoxide production using Ti-UVM-7 porous nanosized catalysts, New J. Chem. 26 (2002) 1093–1095, https://doi.org/10.1039/B205856C.

[54] T. Mosmann, Rapid colorimetric assay for cellular growth and survival: application to proliferation and cytotoxicity assays, J. Immunol. Methods 65 (1983) 55–63, https://doi.org/10.1016/0022-1759(83)90303-4.

[55] L. Garcia-Rodenas, S.J. Liberman, Hydrolysis of gadolinium(III) in light and heavy water, Talanta 38 (1991) 313–318, https://doi.org/10.1016/0039-9140(91)80053-3.

[56] C.F. Baes, R.E. Messmer, The Hydrolysis of Cations, Wiley, New York, 1976.

[57] C.J. Brinker, G.W. Scherer, Sol-Gel Science, the Physics and Chemistry of Sol-Gel Processing, Academic Press, Inc., London, 1990.

[58] I. Mylonas-Margaritis, J. Mayans, S.M. Sakellakou, C.P. Raptopoulou, V. Psycharis, A. Escuer, S.P. Perlepes, Using the singly deprotonated triethanolamine to prepare dinuclear lanthanide(III) complexes: synthesis, structural characterization and magnetic studies, Magnetochemistry 3 (2017) 5, https://doi.org/10.3390/magnetochemistry3010005.

[59] P.S. Koroteev, A.B. Ilyukhin, N.N. Efimov, E.V. Belova, A.V. Gavrikov, V. M. Novotortsev, Mononuclear and binuclear lanthanide acetates with chelating and bridging triethanolamine ligands, Polyhedron 154 (2018) 54–64, https://doi.org/10.1016/j.poly.2018.07.027.

[60] T.N. Hooper, S.K. Langley, S. Gómez-Coca, G. Lorusso, E. Ruiz, K.S. Murray, M. Evangelisti, E.K. Brechin, Coming full circle: constructing a [Gd6] wheel dimer by dimer and the importance of spin topology, Dalton Trans. 46 (2017) 10255–10263, https://doi.org/10.1039/C7DT02281F.

[61] Y. Liu, L. Gao, Low-temperature synthesis of nanocrystalline yttrium aluminum garnet powder using triethanolamine, J. Am. Ceram. Soc. 86 (2003) 1651–1653, https://doi.org/10.1111/j.1151-2916.2003.tb03535.x.

[62] R.K. Iller, The Chemistry of Silica. Solubility, Polymerization, Colloid and Surface Properties, and Biochemistry, John Wiley & Sons, NewYork, 1979.

[63] P. Patnaik, Handbook of Inorganic Chemicals, McGraw-Hill, 2002, ISBN 0-07-049439-8.

[64] J.F. Wall, C.F. Zukoski, Alcohol-induced structural transformations of surfactant aggregates, Langmuir 15 (1999) 7432–7437, https://doi.org/10.1021/la980076x.

[65] D. Attwood, V. Mosquera, J. Rodriguez, M. Garcia, M.J. Suarez, Effect of alcohols on the micellar properties in aqueous solution of alkyltrimethylammonium bromides, Colloid Polym. Sci. 272 (1994) 584–591, https://doi.org/10.1007/BF00653225.

[66] X. Miao, W. Xu, H. Cha, Y. Chang, I.T. Oh, K.S. Chae, T. Tegafaw, S.L. Ho, S.J. Kim, G.H. Lee, Ultrasmall Gd_2O_3 nanoparticles surface-coated by polyacrylic acid (PAA) and their PAA-size dependent relaxometric properties, Appl. Surf. Sci. 477 (2019) 111–115, https://doi.org/10.1016/j.apsusc.2017.11.225.

[67] O. Kahn, Molecular Magnetism, VCH Publishers, New York, 1993 (chapter 2).

[68] C.-C. Huang, T.-Y. Liu, C.-H. Su, T.-W. lo, J.-H. Chen, C.-S. Yeh, Superparamagnetic hollow and paramagnetic porous Gd_2O_3 particles, Chem. Mater. 20 (2008) 3840–3848, https://doi.org/10.1021/cm703195u.

[69] R. Paul, T. Paramanik, K. Das, P. Sen, B. Satpati, I. Das, Magnetocaloric effect at cryogenic temperature in gadolinium oxide nanotubes, J. Magn. Magn Mater. 417 (2016) 182–188, https://doi.org/10.1016/j.jmmm.2016.05.057.

[70] A.T.M. Rahman, K. Vasilev, P. Majewski, Ultra small Gd_2O_3 nanoparticles: absorption and emission properties, J. Colloid Interface Sci. 354 (2011) 592–596, https://doi.org/10.1016/j.jcis.2010.11.012.

[71] M. Rohrer, H. Bauer, J. Mintorovitch, M. Requardt, H. Weismann, Comparison of magnetic properties of MRI contrast media solutions at different magnetic field strengths, J. Invest. Radiol. 40 (2005) 715–724, https://doi.org/10.1097/01.rli.0000184756.66360.d3.

[72] P. Caravan, C.T. Farrar, L. Frullano, R. Uppal, Influence of molecular parameters and increasing magnetic field strength on relaxivity of gadolinium- and manganese-based T1 contrast agents, Contrast Media Mol. Imaging 4 (2009) 89–100, https://doi.org/10.1002/cmmi.267.

[73] Z. Zhou, R. Bai, J. Munasinghe, Z. Shen, L. Nie, X. Chen, T1–T2 dual-modal magnetic resonance imaging: from molecular basis to contrast agents, ACS Nano 11 (2017) 5227–5232, https://doi.org/10.1021/acsnano.7b03075.

[74] C.-S. Yeh, C.-H. Su, W.-Y. Ho, C.-C. Huang, J.-C. Chang, Y.-H. Chien, S.-T. Hung, M.-C. Liau, H.-Y. Ho, Tumor targeting and MR imaging with lipophilic cyanine-mediated near-infrared responsive porous Gd silicate nanoparticles, Biomaterials 34 (2013) 5677–5688, https://doi.org/10.1016/j.biomaterials.2013.04.020.

[75] R.A. Brooks, F. Moiny, P. Gillis, On T2-shortening by weakly magnetized particles: the chemical exchange model, Magn. Reson. Med. 45 (2001), 1014e20, https://doi.org/10.1002/mrm.10064.

[76] I. Gunnarsson, S. Arnorsson, Amorphous silica solubility and the thermodynamic properties of H4SiO40 in the range of 0° to 350°C at Psat, Geochem. Cosmochim. Acta 64 (2000) 2295–2307, https://doi.org/10.1016/S0016-7037(99)00426-3.

[77] W. Vogelsberger, A. Seidel, G. Rudakoff, Solubility of silica gel in water, J. Chem. Soc., Faraday Trans. 88 (1992) 473–476, https://doi.org/10.1039/FT9928800473.

[78] K. Braun, A. Pochert, M. Beck, R. Fiedler, J. Gruber, M. Lindén, Dissolution kinetics of mesoporous silica nanoparticles in different simulated body fluids, J. Sol. Gel Sci. Technol. 79 (2016) 319–327, https://doi.org/10.1007/s10971-016-4053-9.

[79] K. Maciejewska, B. Pozniak, M. Tikhomirov, A. Kobylinska, L. Marciniak, Synthesis, cytotoxicity assessment and optical properties characterization of colloidal $GdPO_4$:Mn^{2+}, Eu^{3+} for high sensitivity luminescent nanothermometers operating in the physiological temperature range, Nanomaterials 10 (2020) 421. https://doi:10.3390/nano10030421.

[80] M. Yon, C. Billotey, J.-D. Marty, Gadolinium-based contrast agents: from gadolinium complexes to colloidal systems, Int. J. Pharm. 569 (2019), 118577, https://doi.org/10.1016/j.ijpharm.2019.118577.